



Project funded by the European Commission under the 6th (EC) RTD Framework Programme (2002- 2006) within the framework of the specific research and technological development programme "Integrating and Strengthening the European Research Area"



Project UpWind

Contract No.: 019945 (SES6)

"Integrated Wind Turbine Design"



Evaluating Wake Models for Use in Complex Terrain

Deliverable 8.3

AUTHOR:	John Prospathopoulos ¹ & Evangelos S. Politis ¹
AFFILIATION:	¹ Centre for Renewable Energy Sources
ADDRESS:	19 th km Marathonos Ave., GR19009, Pikermi, Greece
TEL.:	(+30) 2106603300
EMAIL:	jprosp@cres.gr
FURTHER AUTHORS:	Rebecca J. Barthelmie ² and Daniel Cabezón ³
AFFILIATION:	² University of Edinburgh, ³ National Renewable Energy Centre (Spain)
REVIEWER:	
APPROVER:	

Document Information

DOCUMENT TYPE	Deliverable
DOCUMENT NAME:	D8.3
REVISION:	01
REV. DATE:	February 29, 2008
CLASSIFICATION:	R3: Restricted to WP members
STATUS:	Final

Abstract: This report is the third deliverable of Work Package 8 of the UpWind project. The report deals with the modeling of the wind turbine wakes using a Navier–Stokes solver along with the k - ω turbulence model, where wind turbines are modelled as momentum absorbers. Application is made for two ideal Gaussian hill configurations, one axisymmetric 3D and one quasi-3D, for various turbulence intensity and wind direction conditions. Simulations are made with one wind turbine placed at hilltop and without. The simulations without wind turbine are needed to provide the value of wind speed at the rotor position for the calculation of the actuator disk force, as well as the reference velocity field for the evaluation of the wind speed deficit. Results are presented separately for the cases with and without wind turbine in the form of streamwise wind speed variations at hub height, vertical profiles and wind speed contours. The predictions of the wind speed deficit for the axisymmetric 3D and the quasi-3D hills using two Navier–Stokes algorithms and one commercial software are compared with those in flat terrain for the various levels of turbulence intensity.

Contents

1.	Introduction	4
2.	Definition of test cases: the Gaussian hill	5
3.	The Methodology	6
3.1	The Navier–Stokes solver of CRES (CRES–FlowNS).....	6
3.2	The Navier–Stokes solver of CENER	7
3.3	The WASP algorithm.....	7
4.	Results and discussion	10
4.1	Flow over the hill without wind turbines	10
4.2	Flow over the hill with one wind turbine at the top.....	19
4.3	Wind speed deficit prediction.....	30
5.	Conclusions	46
6.	References.....	47
	Appendix A	48
	Appendix B	49

STATUS, CONFIDENTIALITY AND ACCESSIBILITY							
Status			Confidentiality			Accessibility	
S0	Approved/Released	x	R0	General public	x	Private web site	
S1	Reviewed		R1	Restricted to project members		Public web site	x
S2	Pending for review		R2	Restricted to European. Commission		Paper copy	
S3	Draft for comments		R3	Restricted to WP members + PL			
S4	Under preparation		R4	Restricted to Task members +WPL+PL			

PL: Project leader **WPL:** Work package leader **TL:** Task leader

1. Introduction

This report is the third deliverable of Work Package 8 of the project “Integrated Wind Turbine Design” (UpWind) partially funded by the European Commission under the contract 019945 (SES6). The partners involved in this work package are Risø National Laboratory (Risø, Denmark), Technical University of Denmark (DTU, Denmark), Energy Research Centre of the Netherlands (ECN), Centre for Renewable Energy Sources (CRES, Greece), National Technical University of Athens (NTUA, Greece), Garrad Hassan & Partners Ltd. (GH, England), University of Edinburgh (UEDIN, Scotland) and National Renewable Energy Centre (CENER, Spain).

The overall objective of this work package is to develop a basis for modelling the wake effects in both large off-shore and complex terrain wind farms. The existing engineering type models have been developed and calibrated for flat terrain applications, so their use in complex terrain applications has not been thoroughly validated yet. Taking into account the difficulty to conduct full scale measurements in complex terrain, Navier–Stokes flow modelling can be used for numerical simulations, since, apart from being able of modelling the complex topography, it is capable of taking into account the interaction of a wind turbine (W/T) wake with the wind shear and the narrowing of the wind rose, and therefore can constitute a sound basis for evaluating the features of the wakes in complex terrain and evaluate the existing engineering-type models. The first step towards this direction is to simulate some ideal complex terrain test cases and to compare the predicted wake characteristics with those in flat terrain. To this end, four reference terrain cases have been defined: a 3D axisymmetric and a quasi-3D Gaussian hill, each one with two different mean slopes.

This report deals with the simulation of the 3D axisymmetric and quasi-3D Gaussian hill for the case of the steepest slope. In Chapter 2, the terrain geometry is defined and the test cases are selected for various levels of turbulence intensity and wind direction. In Chapter 3, a short description of the methodology is provided, focusing on the numerical part concerning grid construction and boundary conditions.

Three partners have contributed to the report; CRES, CENER and UEDIN. Numerical predictions of the wind speed and turbulence intensity are presented in Chapter 4, in the form of streamwise variations, vertical profiles and contours, and are distinguished into three sections. The first one refers to the simulations without W/T, which are necessary to estimate the reference wind speed field. The second presents the respective predictions when a reference paper case 5 MW W/T is included in the computation, modelled as an actuator disk at the hill top. Finally, in the third section, the predictions of the wake deficit, calculated as the wind speed difference between the two previous simulations are presented and compared to those in flat terrain for the various cases.

2. Definition of test cases: the Gaussian hill

The idealized simulation of a single wake in the case of a Gaussian hill has been selected as the basis for the comparison of the wake characteristics between flat and complex terrain. The conclusions deduced from the analysis of the axisymmetric and quasi-3D Gaussian hill can be extended to more complex terrain where the irregularities of the topography are seen as separate hills.

The Gaussian quasi-3D hill geometry is defined by the relationship:

$$z = h e^{-0.5 \left(\frac{x}{\sigma} \right)^2}, \quad \sigma = L/1.1774, \quad (1)$$

where x and z are the horizontal and vertical coordinates, h is the height of the hill and L is defined as $x(z = h/2)$. In the case of the axisymmetric hill, $\sqrt{x^2 + y^2}$ replaces x in Eq. (1). The axisymmetric and quasi-3D hill terrain derived from Eq. (1) for $L = 1750$ are shown in Figure 1. The configuration investigated corresponds to $h = 700$ m and $L = 1750$ m (steep slope with a mean value of 0.4).

The different configurations are simulated with one W/T placed at hilltop and without. The simulations without W/T are needed to provide the value of wind speed at the W/T position for the calculation of the actuator disk force, as well as the reference wind speed field for the evaluation of the wind speed deficit. The machine is the reference 5 MW turbine established in WP 1A1 that features a diameter (D) of 126 m and 90 m hub height. The inflow wind speed profile is assumed logarithmic with 500 m boundary layer height and 10 m/s wind speed at hub height. Three different levels of inlet turbulence intensity Tl_{in} at hub height, 5, 13 and 20%, are examined. The different levels of Tl_{in} correspond to different values of roughness length ($2.29 \cdot 10^{-7}$, 0.0445 and 0.639 m, respectively, see Appendix A) and subsequently to different inflow wind speed profiles. All computations are initially carried out for flat terrain using the same grid size to allow for a reliable comparison. For the quasi-3D hill case, three different wind directions, 0, 15° and 30° are also investigated.

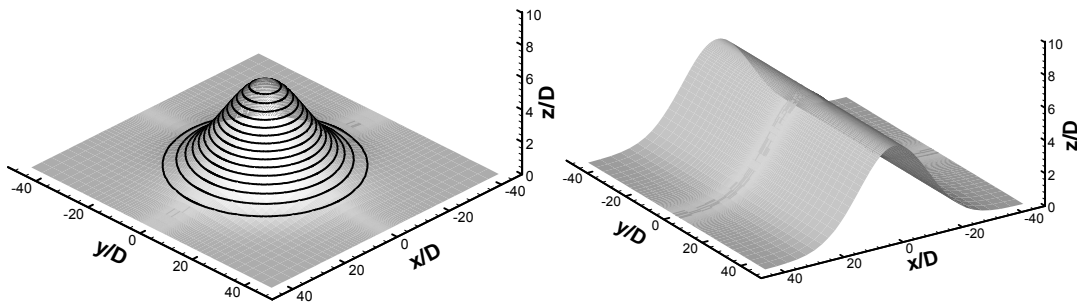


Figure 1: Layout of the terrain for the axisymmetric and the quasi-3D Gaussian hills.

3. The Methodology

For the purposes of this report, two Navier–Stokes solvers (one in-house developed in CRES and one commercial, FLUENT, employed by CENER), as well as one commercial, linear software (WASP) are employed. They are all briefly presented below.

3.1 The Navier–Stokes solver of CRES (CRES–FlowNS)

3.4.1 The algorithm

The governing equations are numerically integrated by means of an implicit pressure correction scheme, where W/Ts are modelled as momentum absorbers by means of their thrust coefficient [1]. A matrix-free algorithm for pressure updating is introduced, which maintains the compatibility of the velocity and pressure field corrections, allowing for practical unlimited large time steps within the time integration process. Spatial discretization is performed on a computational domain, resulting from a body-fitted coordinate transformation, using finite difference/finite volume techniques. The convection terms in the momentum equations are handled by a second order upwind scheme bounded through a limiter. Centred second order schemes are employed for the discretization of the diffusion terms. The Cartesian velocity components are stored at grid-nodes while pressure is computed at mid-cells. This staggering technique allows for pressure field computation without any explicit need of pressure boundary conditions. A linear fourth order dissipation term is added into the continuity equation to prevent the velocity-pressure decoupling. To accommodate the large computational grids needed in most applications for a fair discretization of the topography at hand, a multi-block version of the implicit solver has been developed. Turbulence closure is achieved using the k – ω model [2], with, suitably modified for atmospheric flows, coefficients:

$$\alpha = 0.3706, \quad \beta = 0.0275, \quad \beta^* = 0.033, \quad \sigma = 0.5, \quad \sigma^* = 0.5 \quad (2)$$

3.4.2 Computational domain and grid

Since all computations are run in non-dimensional form, the dimensionalization of lengths and wind speeds has been made with the W/T rotor diameter, D , and the ambient wind speed, U_∞ , respectively. The dimensions of the computational domain have been extended sufficiently so that the flow is not restricted. For the flat terrain cases, the x dimension of the computational domain ranges from $-10D$ to $20D$, the y dimension ranges from $-10D$ to $10D$ and its height is $11D$. For the Gaussian hill cases, the horizontal dimensions x and y range approximately from $-75D$ to $75D$ and the height is $80D$. In each case, the W/T is positioned at the origin of the axes. The distribution of grid-lines is kept the same for all cases. In the horizontal directions, the grid size is constant, equal to $0.05D$, from $-0.55D$ to $0.55D$ (around the W/T), and increases outwards, following a geometrical progression, until the maximum dimension of the domain is reached (see Figure 2). In the vertical direction, the first three grid-lines are positioned close to the ground at heights 0.01 , 0.03 and $0.05D$ respectively. From $0.05D$ up to a height of $1.55D$ the grid size is kept constant, equal to $0.05D$, and then increases following a geometrical progression up to the maximum height of the domain. In this way, a fine mesh is constructed in the area of the W/T (see Figure 3).

If the wind direction is not parallel to the x -axis, the disk rotor is rotated by a yaw angle to remain perpendicular to the flow. This angle is the wind speed direction at the W/T's rotor centre, as calculated from the simulation without W/T. In such a case, the horizontal grid mesh is modified, as shown in Figure 4, so that the grid lines are aligned with the plane of the yawed disk rotor.

3.4.3 Boundary conditions

The inflow wind speed profile follows the logarithmic law:

$$U_x = \frac{u_*}{K} \ln\left(\frac{z}{z_0}\right), \quad (3)$$

where u_* is the friction velocity, $K=0.41$ is the von-Karman constant and z_0 is the

roughness length. In the case of inflow not aligned with x direction, Eq. (2) takes the form:

$$U_x = \frac{u_*}{K} \ln\left(\frac{z}{z_0}\right) \cos(a_w), \quad U_y = \frac{u_*}{K} \ln\left(\frac{z}{z_0}\right) \sin(a_w), \quad (4)$$

where a_w is the wind direction relative to x-axis.

The friction velocity is related to the roughness through:

$$u_* = \frac{K}{\ln(\delta / z_0)}, \quad (5)$$

with δ being the atmospheric boundary layer thickness and $U_x(\delta) = 1$. The inflow k and ω profiles are given by the relationships:

$$k = u_*^2 / \sqrt{\beta_*}, \quad \omega = \frac{u_*}{\sqrt{\beta_*} K z} \quad (6)$$

On the lower surface, the non-slip condition yields zero wind speed. The Cartesian wind speed components are specified at the upper far-field boundary ($U_x = 1, U_y = 0, U_z = 0$). Neumann wind speed conditions are imposed at the outflow and the side boundaries. For the boundary conditions of k and ω , a similar approach is followed. It must be noted that Neumann conditions are imposed at the inlet plane as well, allowing k and ω to adapt themselves to the prescribed boundary conditions.

3.2 The Navier–Stokes solver of CENER

The model is based on the commercial CFD code Fluent, adapted for the calculation of the local effects on complex terrain in the neutral atmospheric boundary layer. Wind is considered as 3D incompressible steady flow and the Coriolis force as well as the heat effects are omitted.

The modified Navier–Stokes equations are averaged by decomposing the instantaneous velocity into a mean and a fluctuating value, solved through the Reynolds stress tensor. The model is based on the standard k – ϵ turbulence closure scheme, which includes the Boussinesq hypothesis in order to relate the Reynolds Stress Tensor to the velocity gradients through the eddy viscosity concept.

The inlet boundary conditions are based on the profiles of wind speed, turbulent kinetic energy and turbulent dissipation rate, as solution of the k – ϵ model in the turbulent surface boundary layer considering local equilibrium at the wall.

The terrain is parameterized as a rough wall according to the local aerodynamic roughness length and it is solved by using modified wall functions adapted to the logarithmic wind speed profile of the atmospheric boundary layer.

The mesh is created through a semi-automatic grid generator based on block topologies in order to generate structured meshes projected onto the surface of the terrain.

The wake model is based on the actuator-disk concept. The turbine is represented by an actuator disk upon which a distribution of forces, defined as axial momentum sources, are applied on the incoming flow at a rate defined by the work that the rotor extracts from the fluid. The rotor is supposed to be uniformly loaded, with the exerted forces as a function of the incident wind speed, the thrust coefficient and the rotor diameter.

3.3 The WAsP algorithm

The Wind Atlas Analysis and Application Program (WAsP) is based on a linearised model used in the European Wind Atlas [3]. The WAsP program [4] uses meteorological data from a measurement station to generate a local wind climate from which the effects of obstacles, roughness and complex terrain have been removed. To produce a wind climate for a nearby wind farm or wind turbine site these local effects are reintroduced.

WAsP utilises the 'BZ-model' of Troen [5] to calculate the wind velocity perturbations induced by orographic features such as single hills or more complex terrain. The BZ-model belongs to a family of models related to the Jackson and Hunt theory for flow over hills [6][7]. The model was developed with the specific purpose of detailed wind energy siting in mind and has the following general features:

- It employs a high-resolution, zooming, polar grid. This is coupled with a map analysis routine in order to calculate the potential flow perturbation profile at the central point of the model.
- It integrates the roughness conditions of the terrain surface into the spectral or scale decomposition. The 'inner-layer' structure is calculated using a balance condition between surface stress, advection and the pressure gradient.
- It uses an atmospheric boundary layer thickness of approx. 1 km to force the large scale (say, more than a few kilometres) flow around high-elevation areas.

The main advantage of the program is that it is fast and robust. It does not model flow in complex terrain if flow separation occurs although there are methods for improving its predictions in complex terrain [8]. For the simulations discussed below it is important to note that the program is being used in a way which is not recommended. WAsP does not treat the near-wake (less than 3-4 rotor diameters) downstream and these results should be disregarded. Also, the program is being run with a standard wake decay coefficient of 0.075 regardless of the turbulence intensity (which in turn is set by changing the roughness length). The wake decay coefficient defines wake expansion which is related to turbulence intensity so using one standard value for all simulations has an impact on the final results.

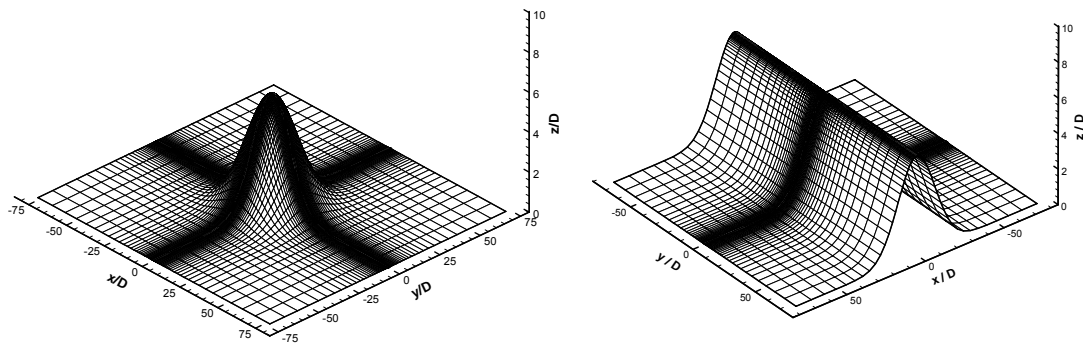


Figure 2: Layout of the generated surface grids for the axisymmetric and the quasi-3D Gaussian hills

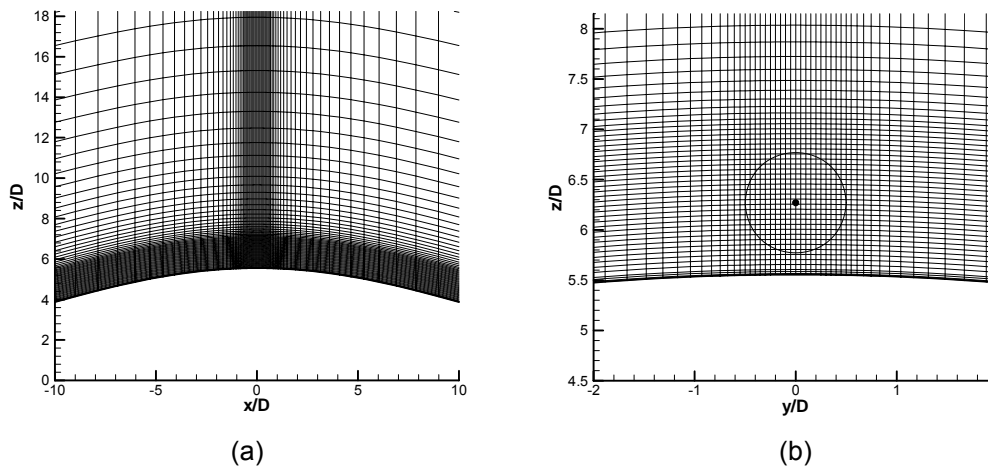


Figure 3: Layout of the grid focusing on the W/T region for the axisymmetric Gaussian hill: (a) at plane $y=0$ and (b) at plane $x=0$

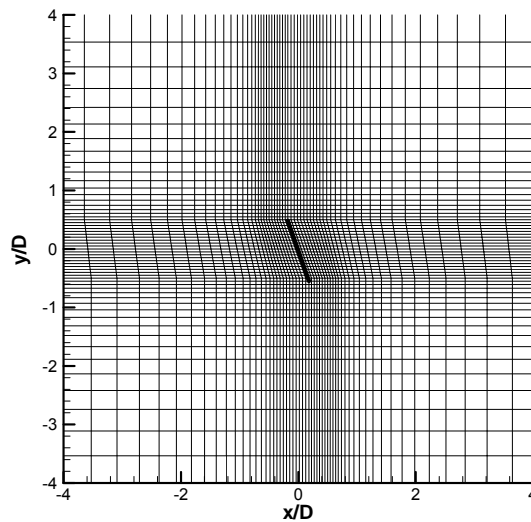


Figure 4: Ground plan of the xy plane at hub height focusing on the region of the yawed disk rotor

4. Results and discussion

4.1 Flow over the hill without wind turbines

The configuration of the hill without W/T is used as a datum test case, since it provides the reference wind speed for the calculation of the deficit and the estimation of the thrust coefficient (C_t) value of the W/T rotor and illustrates the basic flow features in complex terrain. In the following, numerical predictions of the wind speed and the turbulence intensity (TI) are presented. The relationship for the calculation of TI is derived in Appendix B, in connection with [9].

4.1.1 Streamwise variations at hub height

The streamwise variation of the normalized streamwise wind speed (U_x) at hub height for the 3D axisymmetric and the quasi-3D hill is shown in Figure 5a and b, respectively. It is observed that the increase in TI_{in} , which is equivalent to an increase in roughness, results in a higher flow acceleration on the hill top and also a higher deceleration in the lee side of the hill.

It should be noted that for all cases the inflow wind speed at hub height is 10 m/s. However, the variation of roughness modifies the shape of the boundary layer and, consequently, the value of the free stream wind speed. In Table 1, the values of the free stream wind speed U_∞ , along with the corresponding TI_{in} and roughness lengths, are quoted. Dimensionalization with U_∞ explains the different values of inlet wind speed appearing in Figure 5.

Table 1: Dependence of the free stream wind speed on TI_{in}

TI_{in}	z_0 (m)	U_∞ (m/s)
5%	$2.29 \cdot 10^{-7}$	10.90
13%	0.0445	12.47
20%	0.639	13.80

The predicted accelerations and decelerations are higher for the quasi-3D hill. For the quasi-3D case the effect of changing wind direction from 0° to 15° and then 30° is also examined. The presence of the hill changes the initial wind direction leading to a successive decrease by 5° and 10° at the W/T rotor centre. The predicted directions of 10° and 20° at the rotor centre define the axes along which the wind speed variations are calculated. As depicted by Figure 6, there is a small decrease of the predicted accelerations and decelerations when the wind direction changes to 30° . This is a result of the fact that the flow follows a slightly smoother effective terrain course with the change in wind direction.

The predicted variation of turbulence intensity is shown in Figure 7 and Figure 8. Turbulence intensity decreases on the hill top and then reaches its peak in the region of highest wind speed deceleration. For high roughness values ($TI_{in} = 20\%$), the peak in the lee side of the hill reaches more than twice the inlet value. These values become even higher in the quasi-3D case (see Figure 7b). The change in the wind direction from 0° to 30° results in a decrease of the turbulence intensity in the lee side of the hill because of the flow following a smoother course as mentioned in the previous paragraph (Figure 8). This effect becomes significant for high values of roughness ($TI_{in} = 20\%$, see Figure 8c).

The predictions of CRES (Navier–Stokes) and UEDIN (WAsP) for the wind speed at hub height are compared in Figure 9. Normalization of wind speed refers to the velocity at the hill top. As expected WAsP predicts higher flow acceleration at the hill top than the Navier–Stokes code.

Both codes agree that flow acceleration increases with TI_{in} , however flow deceleration is not so well reproduced by WASP at the lee side of the hill.

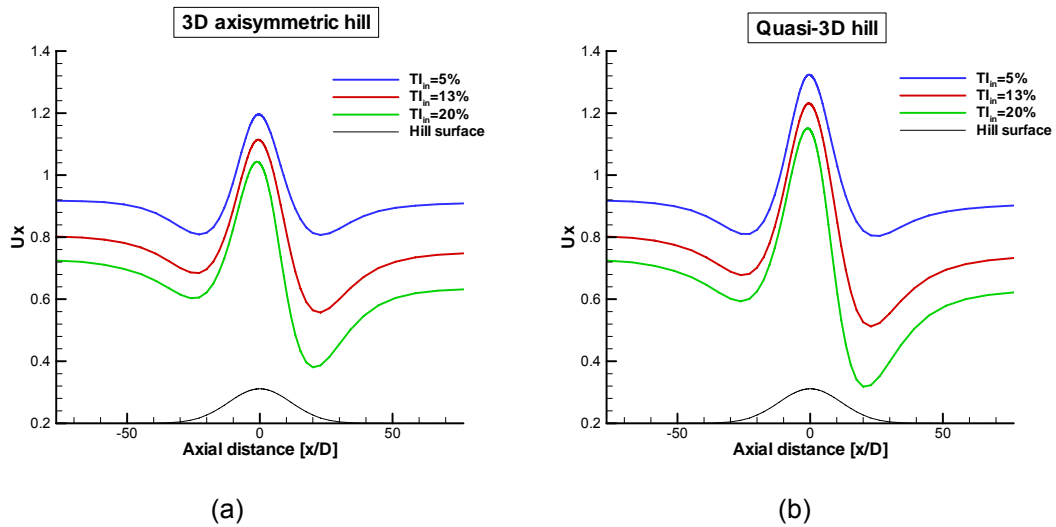


Figure 5: Variation of the streamwise wind speed at the hub height of the symmetry plane ($y = 0$) for various values of TI_{in} . Wind direction is 0° .

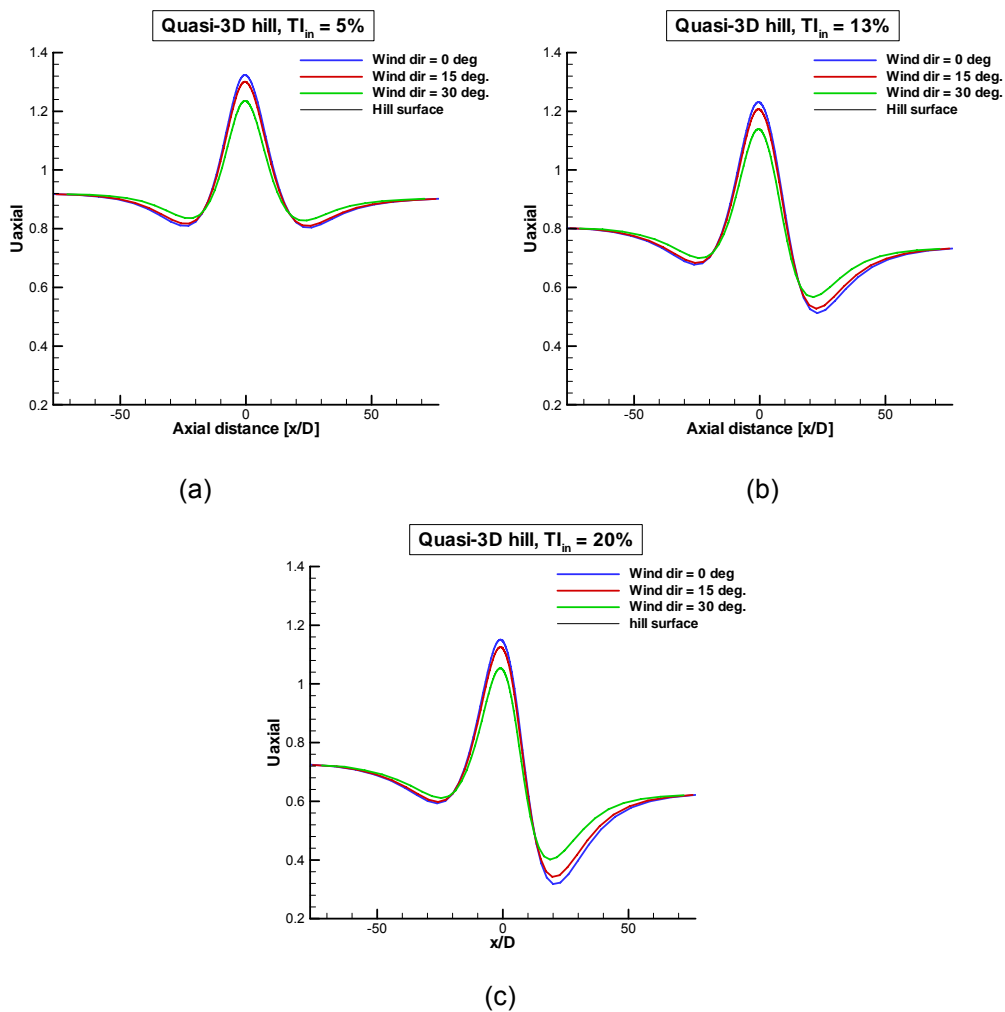


Figure 6: Variation of the streamwise wind speed at the hub height of the symmetry plane ($y = 0$) for various wind directions and TI_{in} values: (a) 5%, (b) 13% and (c) 20%.

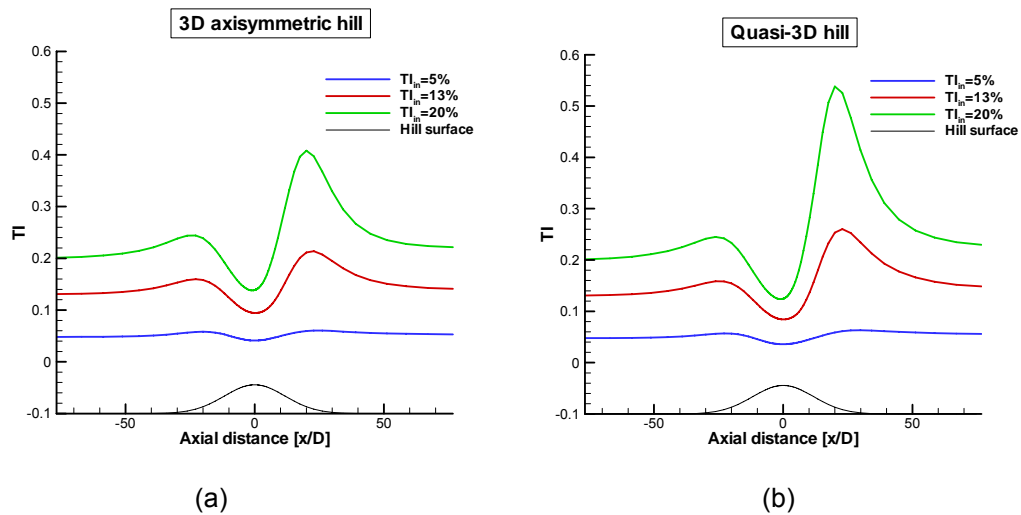


Figure 7: Variation of the turbulence intensity at the hub height of the symmetry plane ($y = 0$) for various values of TI_{in} values. Wind direction is 0° .

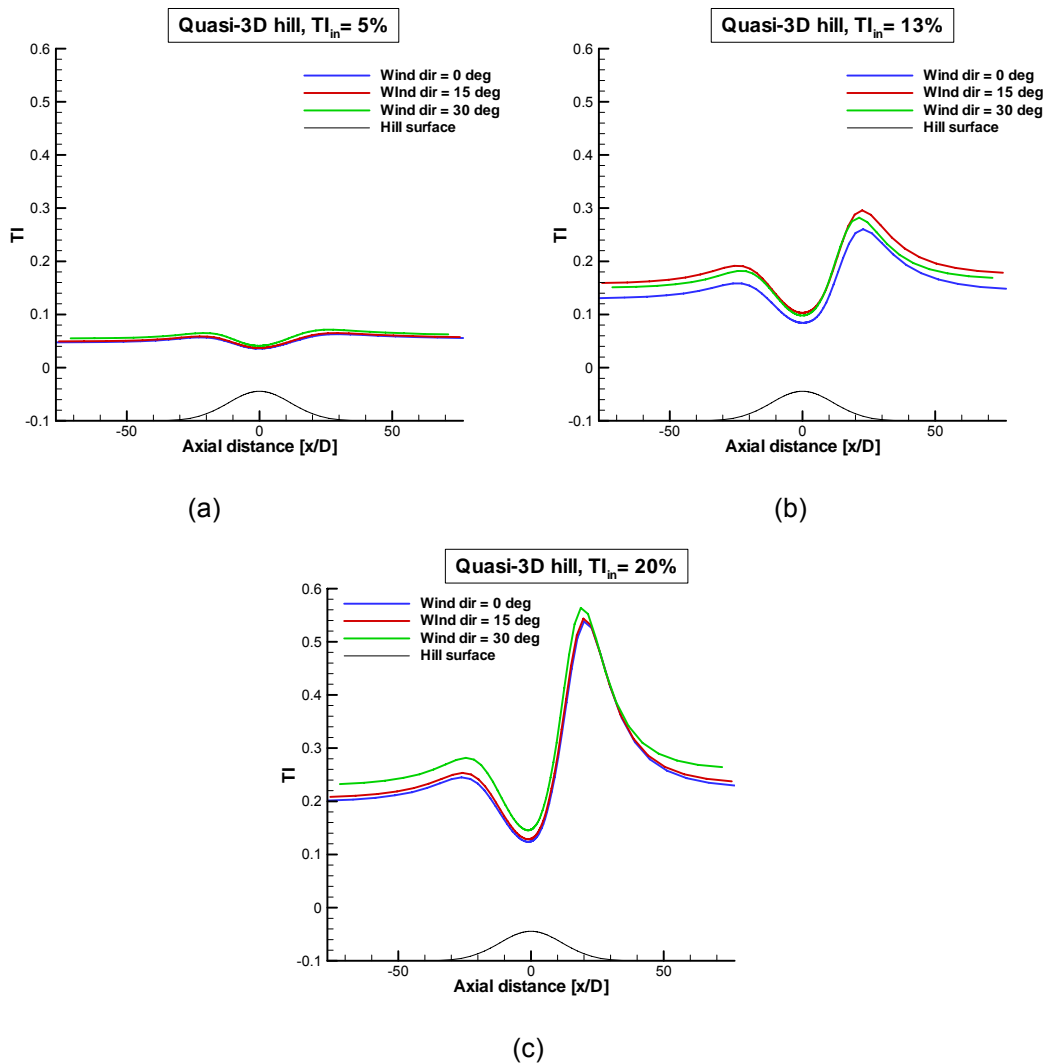


Figure 8: Variation of the turbulence intensity at the hub height of the symmetry plane ($y = 0$) for various wind directions and TI_{in} values: (a) 5%, (b) 13% and (c) 20%.

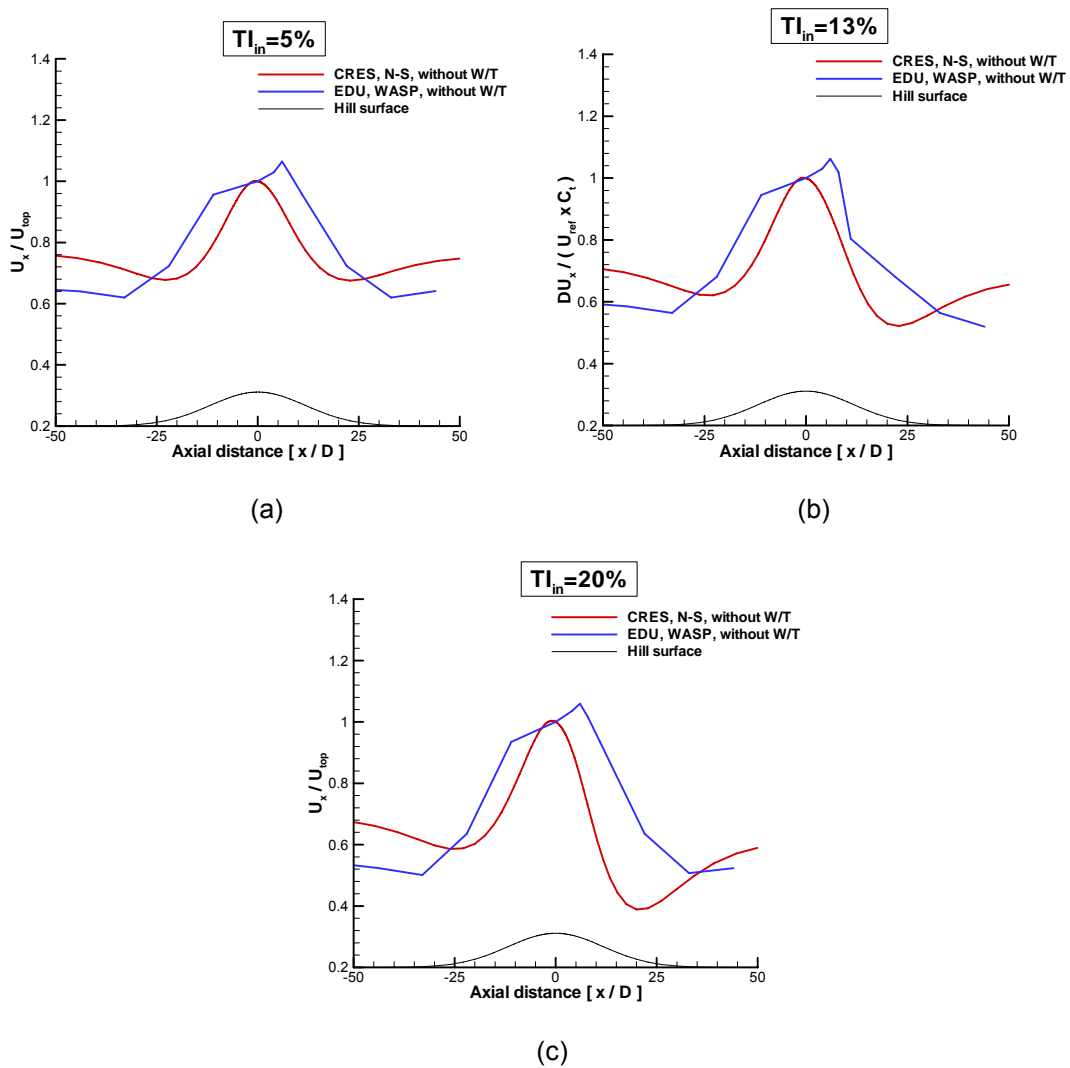


Figure 9: 3D axisymmetric hill - Streamwise wind speed variation at the hub height of the symmetry plane ($y = 0$) for various TI_{in} values: (a) 5%, (b) 13% and (c) 20%. Normalization has been done with the predicted velocity at the hill top (hub height) without W/T.

4.1.2 Vertical profiles

The vertical profiles of U_x component of the wind speed vector are shown in Figure 11 for various distances downstream the hill top. Plotting positions have been selected to cover regions of near and far wake in the presence of a W/T. In the absence of a W/T, the first three positions, $x = 1$, 3 and $5D$ are located in the region of highest flow acceleration, $x = 10D$ is an intermediate position, $x = 20D$ is the position of the highest flow deceleration and $x = 40D$ is located at the hill base, where the terrain has become flat.

The conclusions drawn from the streamwise variations presented in the previous paragraph are also confirmed from the vertical profiles. As depicted by Figure 10 the flow acceleration is observed near the hill top ($1-5D$) and the maximum flow deceleration occurs at $x = 20D$. The deceleration is higher for $TI_{in} = 20\%$. At $x = 40D$, the boundary layer has recovered its logarithmic shape (with higher thickness though) for the lowest $TI_{in} = 5\%$, but it is still in deceleration for $TI_{in} = 20\%$. The comparison of the vertical profiles between axisymmetric and quasi-3D hill indicates the higher acceleration and deceleration for the second case.

The change in wind direction does not significantly affect the wind speed profiles. The slight decrease of the maximum flow acceleration observed in the streamwise variations of Figure 6 is also observed in the vertical profiles of Figure 11 for $x = 1, 3$ and $5D$. The vertical profiles of turbulence intensity presented in Figure 12 and Figure 13 show the significant increase of turbulence in the region of flow deceleration. The level of turbulence intensity remains well above its inlet value even at $40D$ downstream the hill top.

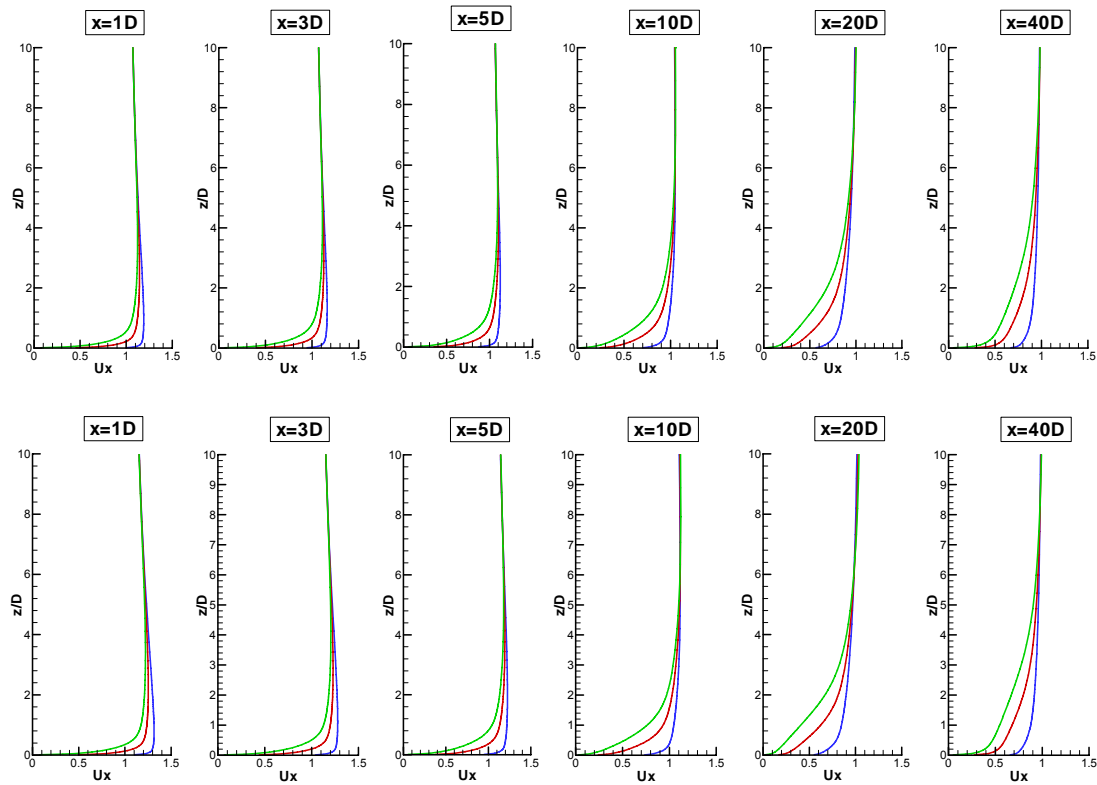


Figure 10: Vertical profiles of the streamwise wind speed downstream the hill top for various values of TI_{in} : — 5%, — 13%, — 20%. Upper: 3D axisymmetric hill. Lower: Quasi-3D hill (wind direction 0°).

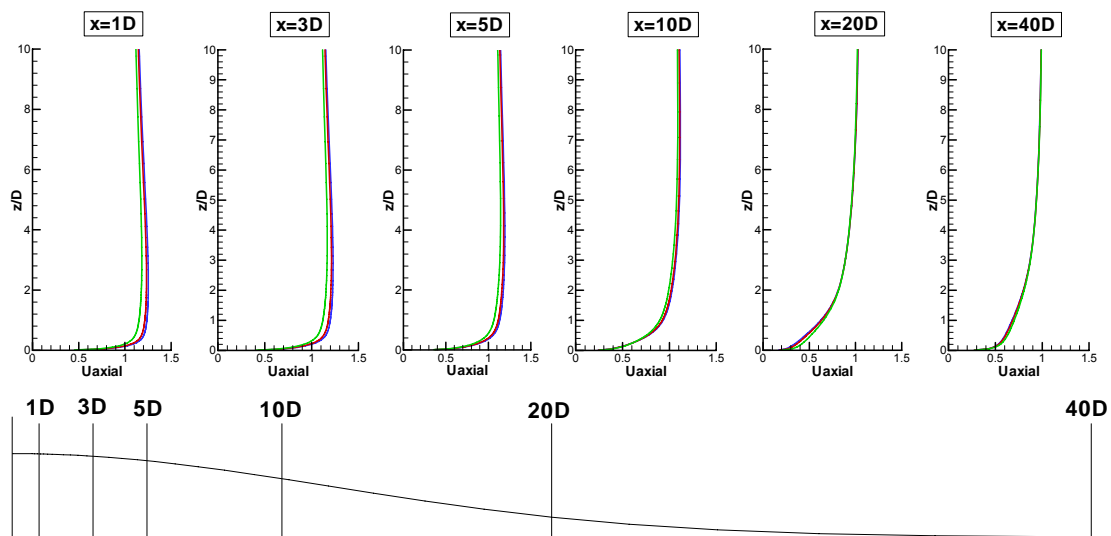


Figure 11: Vertical profiles of the streamwise wind speed downstream the hill top of the quasi-3D hill for various wind directions: — 0° , — 15° , — 30° . TI_{in} is 13%.

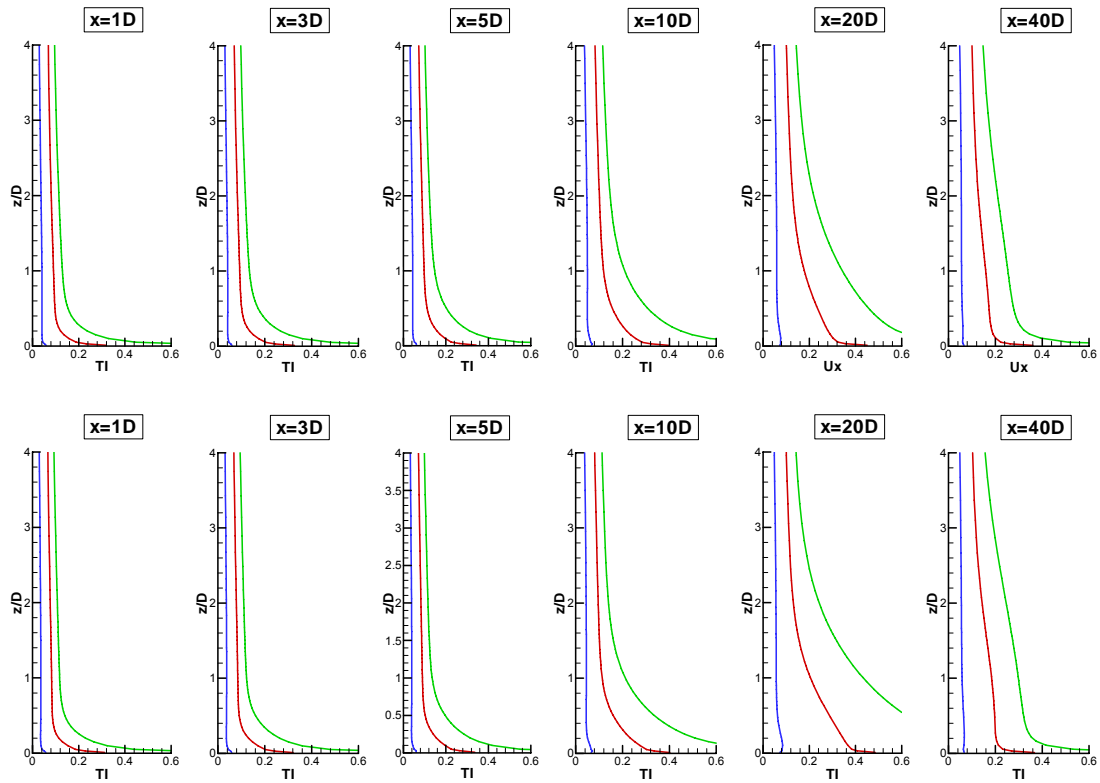


Figure 12: Vertical profiles of the turbulence intensity downstream the hill top for various values of Ti_{in} : — 5%, — 13%, — 20%. Upper: 3D axisymmetric hill. Lower: Quasi-3D hill (wind direction is 0°).

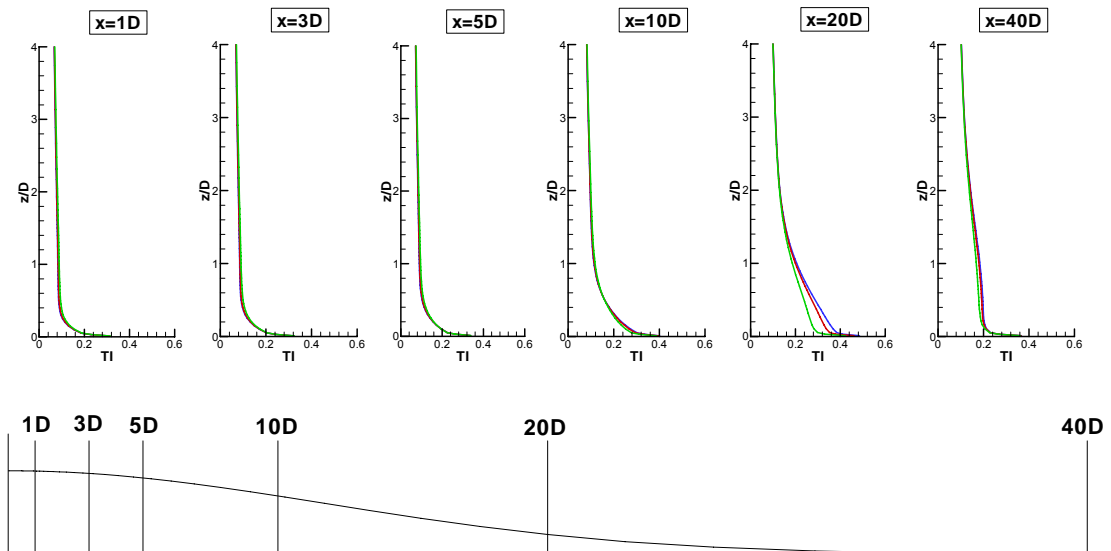


Figure 13: Vertical profiles of the turbulence intensity downstream the hill top of the quasi-3D hill for various wind directions: — 0° , — 15° , — 30° . Ti_{in} is 13%.

The predictions between CRES and UEDIN for the vertical streamwise velocity profiles downstream of the hill top are compared in Figure 14. Normalization of velocity refers to the hill top velocity at hub height. The results at distances 6-11D confirm that WAsP predicts lower flow deceleration at the lee side of the hill. The agreement on the profile gradients can be considered good at all distances.

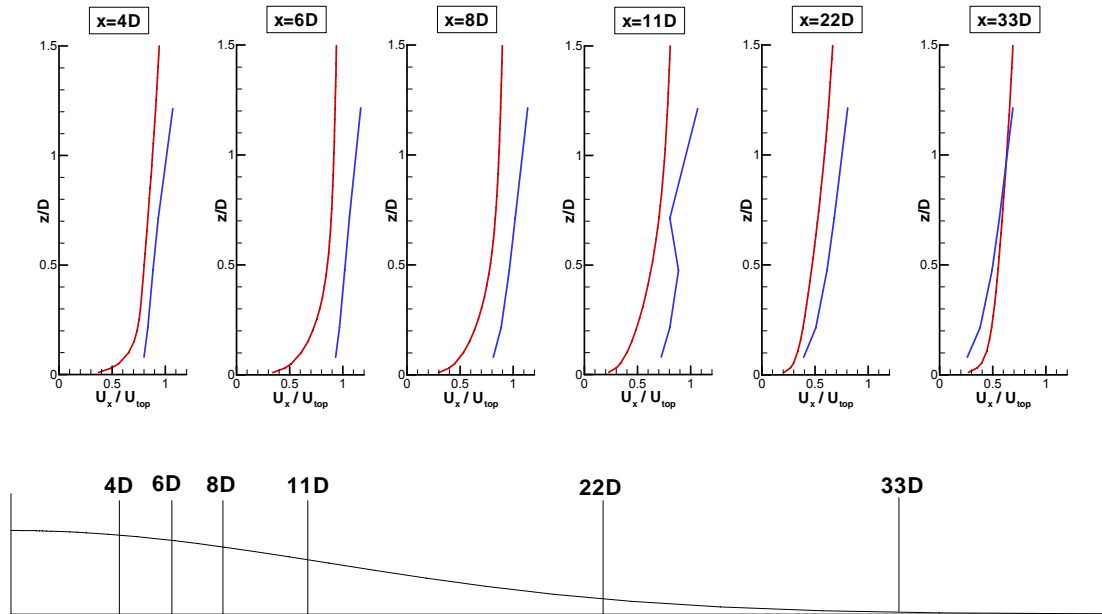


Figure 14: Vertical profiles of the streamwise velocity downstream the hill top of the 3D axisymmetric hill for various distances. — UEDIN (WAsP), — CRES (N-S). Tl_{in} is 13%. Normalization has been done with the predicted velocity at the hill top (hub height).

4.1.3 Wind speed contours

The wind speed contours of the streamwise wind speed at the plane $y = 0$ are compared between the axisymmetric and the quasi-3D hill in Figure 15 for the three Tl_{in} levels considered. The comparison confirms that the wind speed around the hill top are higher in the quasi-3D case than the axisymmetric one. The symmetry of the wind speed pattern around the hill top indicates the full convergence of the numerical code. In Figure 16, the same comparison is made for the U_x wind speed contours at the hub height plane a. g. l. A symmetrical and a 2D-like patterns are clearly observed in the axisymmetric and quasi-3D cases, respectively. The higher accelerations and decelerations in the quasi-3D case are also clearly presented here.

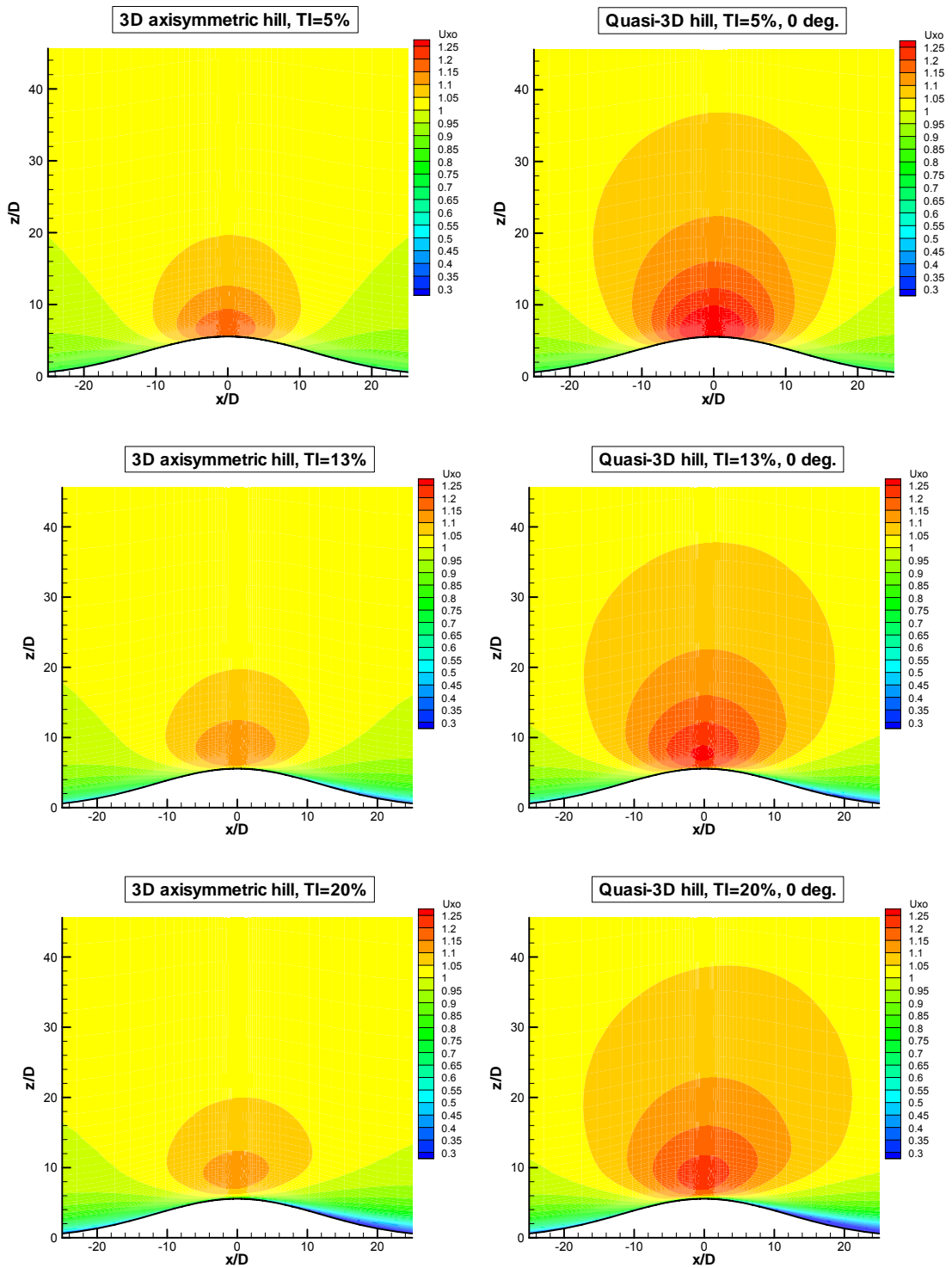


Figure 15: Streamwise wind speed contours for the axisymmetric and quasi-3D hill at the symmetry plane ($y = 0$). Upper: $TI_{in} = 5\%$. Middle: $TI_{in} = 13\%$. Lower: $TI_{in} = 20\%$.

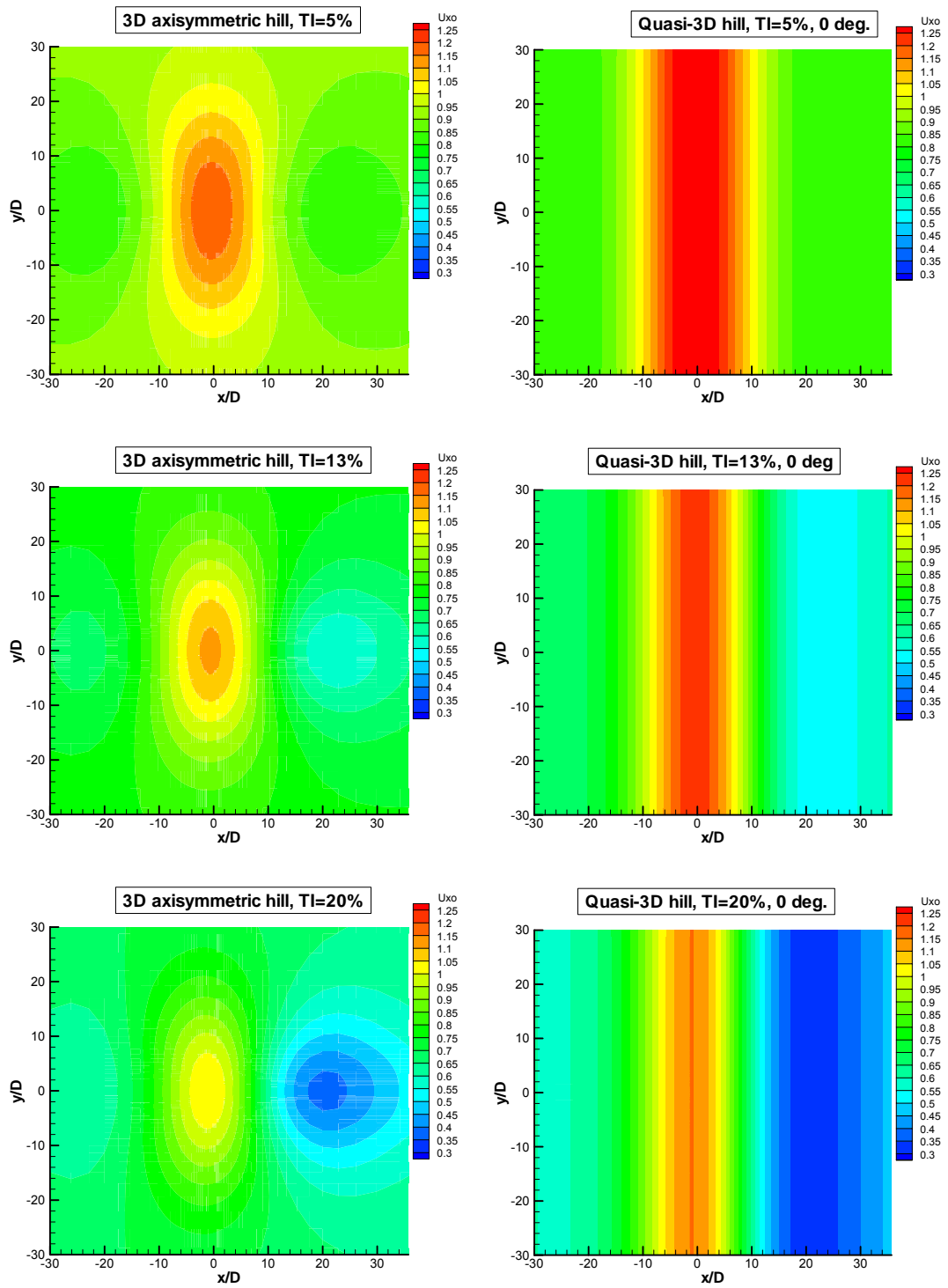


Figure 16: Streamwise wind speed contours for the axisymmetric and quasi-3D hill at hub height a. g. l. Upper: $TI_{in} = 5\%$. Middle: $TI_{in} = 13\%$. Lower: $TI_{in} = 20\%$.

4.2 Flow over the hill with one wind turbine at the top

The presence of the W/T is simulated as a momentum sink at the grid cells that correspond to the disk rotor surface. The source term added to the right hand-side of the momentum equation in x-axis expresses the force exerted on the fluid by the disk rotor:

$$F_{disk} = -\frac{1}{2} \rho U_{disk}^2 C_t A, \quad (7)$$

where ρ is the air density, A is the disk rotor surface, U_{disk} is the reference wind speed at hub height (which obtained from the respective case without W/T) and C_t is the thrust coefficient that corresponds to U_{disk} through the $C_t = f(U)$ curve of the W/T. In Eq. (7), U_{disk} and C_t have been approximated as constant across the disk surface. In Table 2, the predicted reference velocities U_{disk} for the various cases without W/T and the corresponding C_t values are quoted. The values of U_∞ for the different Tl_{in} values are also included in Table 2.

Table 2: Reference velocities and thrust coefficients for the calculation of the W/T force in the various cases examined

Tl_{in}	U_∞	Axisymmetric hill	Quasi-3D hill		
			0°	15°	30°
5%	10.90 m/s	$U_{disk} = 1.19 U_\infty$ $C_t = 0.392$	$U_{disk} = 1.32 U_\infty$ $C_t = 0.281$	$U_{disk} = 1.3 U_\infty$ $C_t = 0.296$	$U_{disk} = 1.23 U_\infty$ $C_t = 0.354$
13%	12.47 m/s	$U_{disk} = 1.11 U_\infty$ $C_t = 0.317$	$U_{disk} = 1.23 U_\infty$ $C_t = 0.230$	$U_{disk} = 1.20 U_\infty$ $C_t = 0.246$	$U_{disk} = 1.14 U_\infty$ $C_t = 0.317$
20%	13.80 m/s	$U_{disk} = 1.04 U_\infty$ $C_t = 0.286$	$U_{disk} = 1.15 U_\infty$ $C_t = 0.210$	$U_{disk} = 1.12 U_\infty$ $C_t = 0.225$	$U_{disk} = 1.05 U_\infty$ $C_t = 0.278$

4.2.1 Streamwise variations at hub height

The impact of Tl_{in} and hill geometry on the development of the streamwise wind speed are similar to those observed in the case without W/T. However, the W/T presence causes an abrupt drop of the wind speed at the disk rotor position, as seen in Figure 17. In the quasi-3D hill case, the differences in acceleration and deceleration produced by changing the wind direction are reinforced with the presence of W/T (see Figure 18). The same applies for the turbulence intensity variations (see Figure 19 and Figure 20). It must be noted that in Figure 18, the U_{axial} has been calculated along the axis defined by the predicted flow direction at rotor's centre in the respective case without W/T. In Figure 21, the streamwise wind speed and turbulence variations are compared for the cases with and without W/T. Apart from the expected differences in the W/T region, an increase in the flow deceleration combined with an increase in turbulence intensity are observed at the lee side of the hill. This effect is more pronounced for the cases with low Tl_{in} and weakens as the level of Tl_{in} increases.

The predictions of the streamwise wind speed at hub height are compared between CRES and UEDIN in Figure 22. Normalization refers to the predicted velocity at hill top without W/T. Both codes predict the abrupt velocity reduction due to the actuator disk. However, the coarse discretization in WAsP results does not permit an accurate comparison of the predicted velocity reductions. The comparison of the predictions behind the W/T is similar to that of Figure 9, without the W/T, indicating the dominant effect of the terrain on the velocity variation.

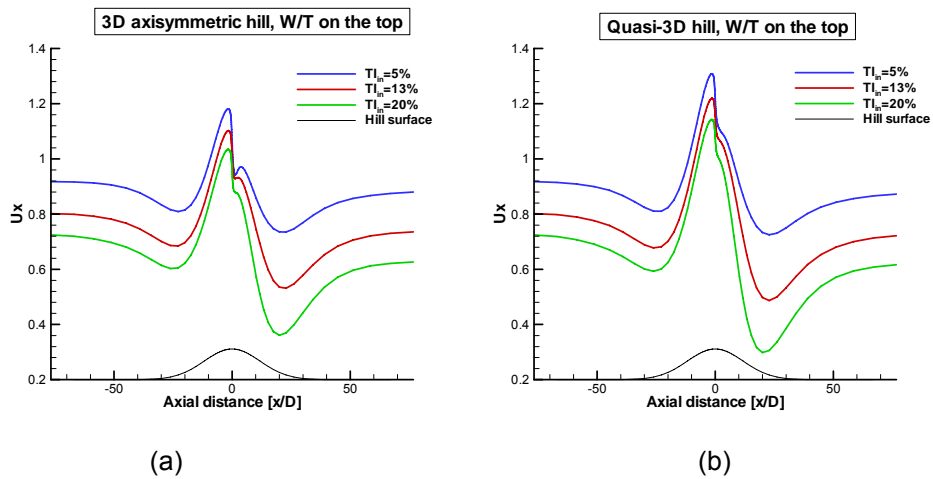


Figure 17: Variation of the streamwise wind speed at the hub height of the symmetry plane ($y = 0$) for various values of TI_{in} . Wind direction is 0° .

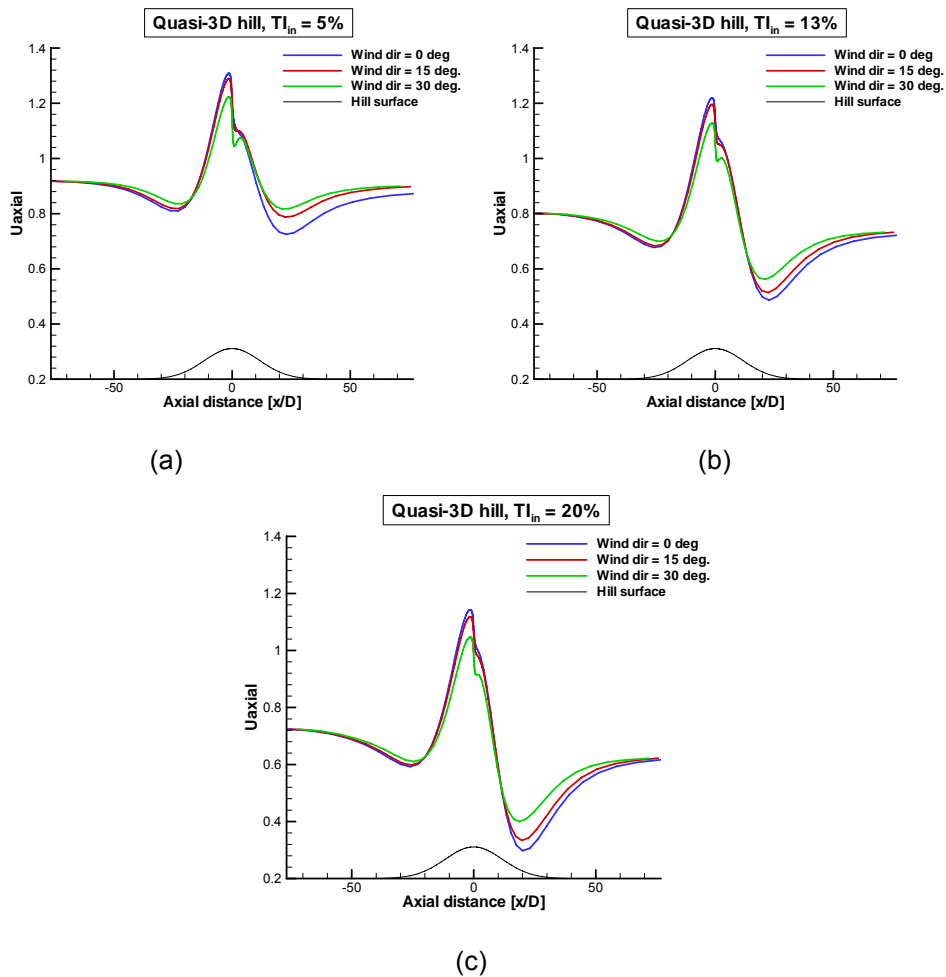


Figure 18: Variation of the streamwise wind speed at the hub height of the symmetry plane ($y = 0$) for various wind directions and TI_{in} values: (a) 5%, (b) 13% and (c) 20%.

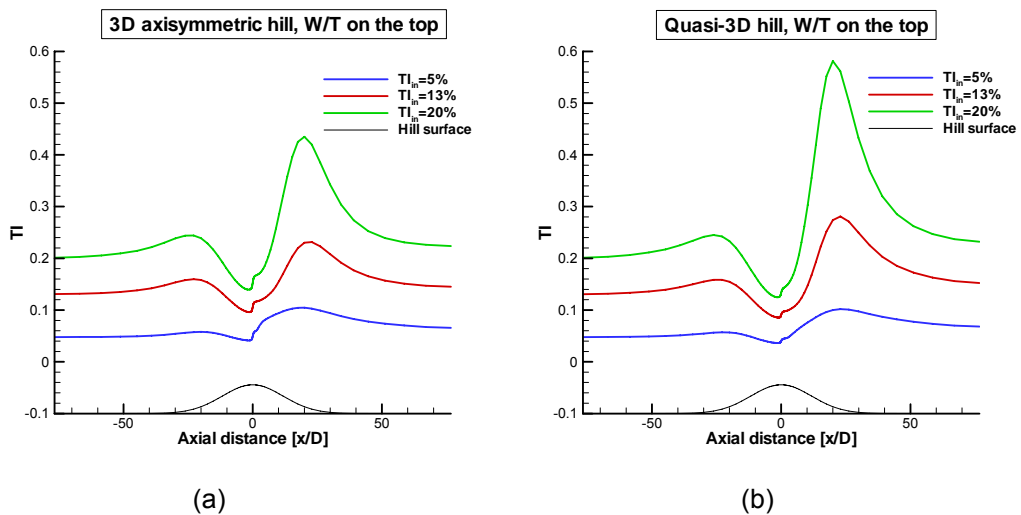


Figure 19: Variation of the turbulence intensity at the hub height of the symmetry plane ($y = 0$) for various values of TI_{in} . Wind direction is 0° .

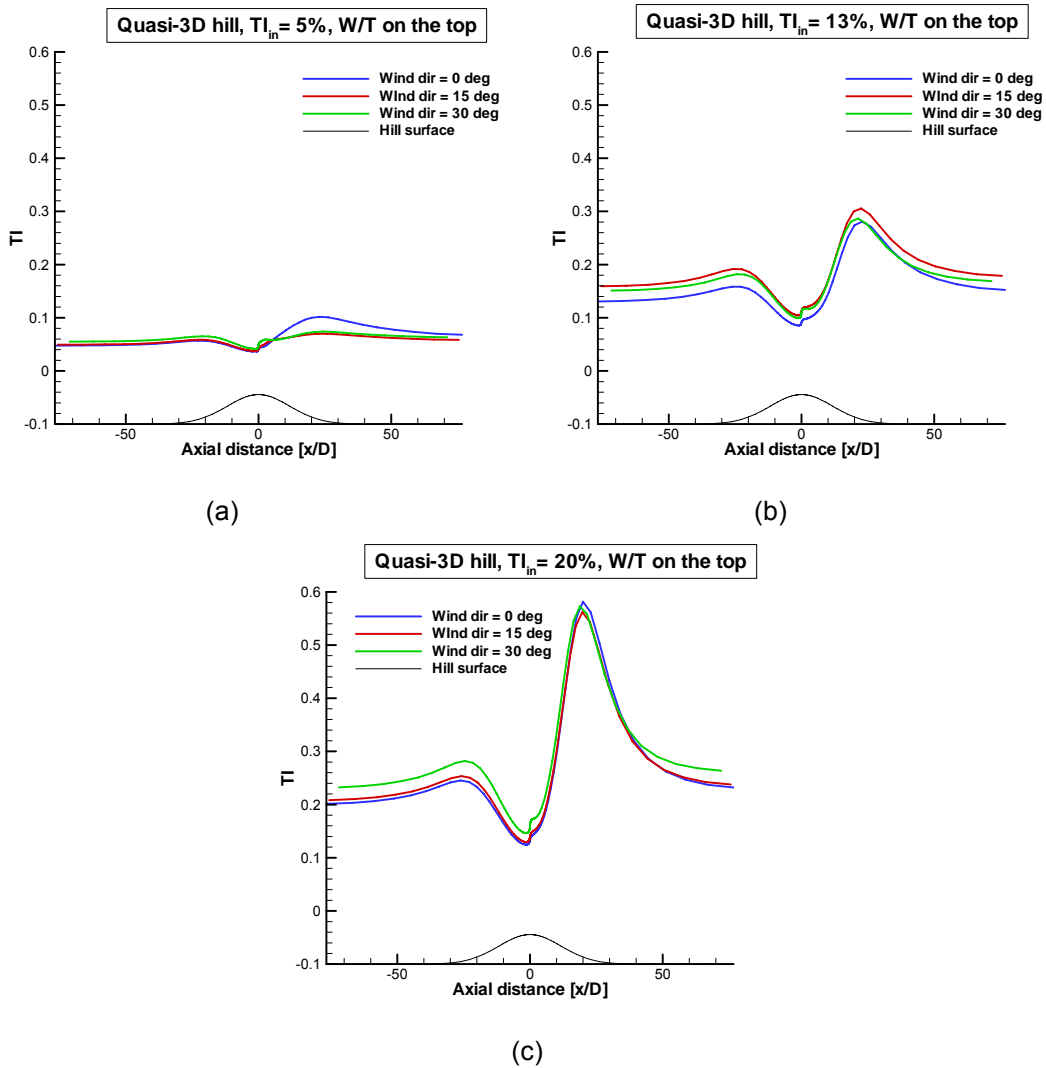


Figure 20: Variation of the turbulence intensity at the hub height of the symmetry plane ($y = 0$) for various wind directions and TI_{in} values: (a) 5%, (b) 13% and (c) 20%.

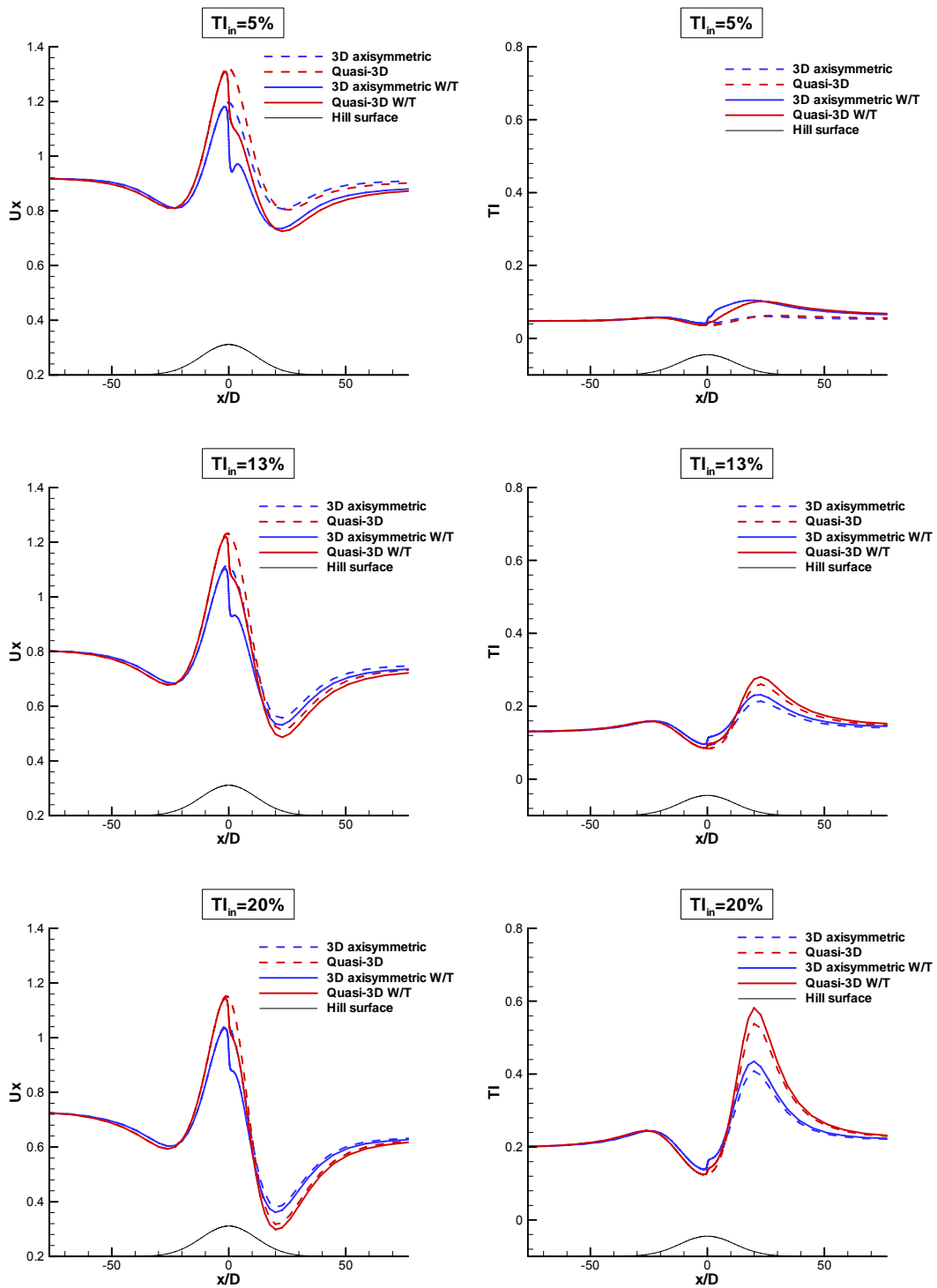


Figure 21: Comparison of the streamwise wind speed and turbulence intensity variation at the hub height of the symmetry plane ($y = 0$) for the axi-symmetric and quasi-3D hills with and without W/T. Upper: $TI_{in} = 5\%$. Middle: $TI_{in} = 13\%$. Lower: $TI_{in} = 20\%$.

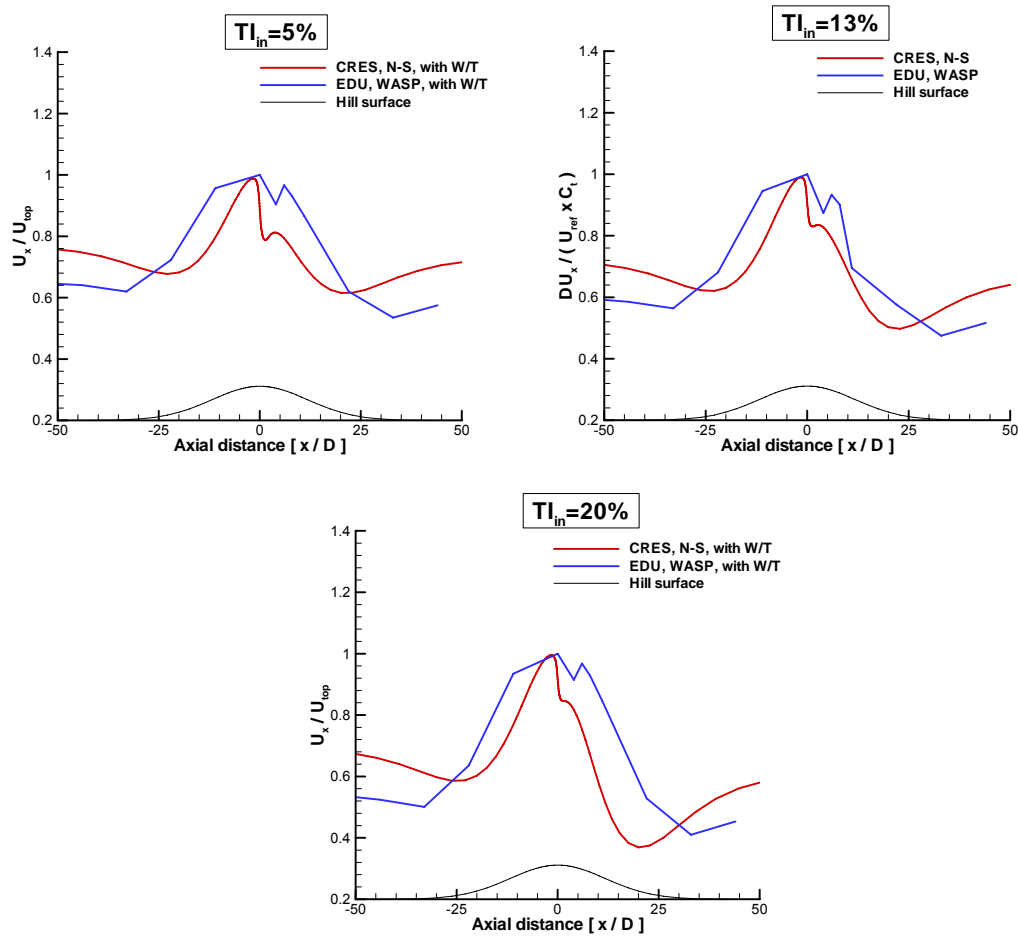


Figure 22: Streamwise wind speed variation at the hub height of the symmetry plane ($y = 0$) for 3D axisymmetric hill for various TI_{in} values: (a) 5%, (b) 13% and (c) 20%.

Normalization has been done with the predicted velocity at the hill top (hub height) without W/T.

4.2.2 Vertical profiles

The W/T induced wake changes the wind speed profile, as depicted by Figure 23 and Figure 24. The change in the shape of the wind speed profile is more pronounced for low turbulence (5%). After $5D$, the distortion of the profile disappears; however there is a delay in the flow recovery compared to the case without W/T. This difference in wind speed between the cases with and without W/T expresses the wind speed deficit in the presence of a W/T. A relative distortion appears in the turbulence intensity profiles (see Figure 25 and Figure 26). As expected, the W/T presence increases the turbulence level behind the machine.

In Figure 27, the predictions of the vertical profiles of the streamwise wind speed are depicted for both CRES and UEDIN. Normalization refers to the velocity at hill top without W/T. The good agreement between the velocity profiles at the distance of $4D$ shows that the simulation of the W/T effect is equivalent in both codes. The comparison of the profile gradients is still satisfactory in the presence of the W/T, although the coarse discretization of the WASP results is not proper for accurate conclusions. At the distance of $33D$, the comparison of the velocity profiles indicates that the Navier–Stokes code predicts a faster flow recovery.

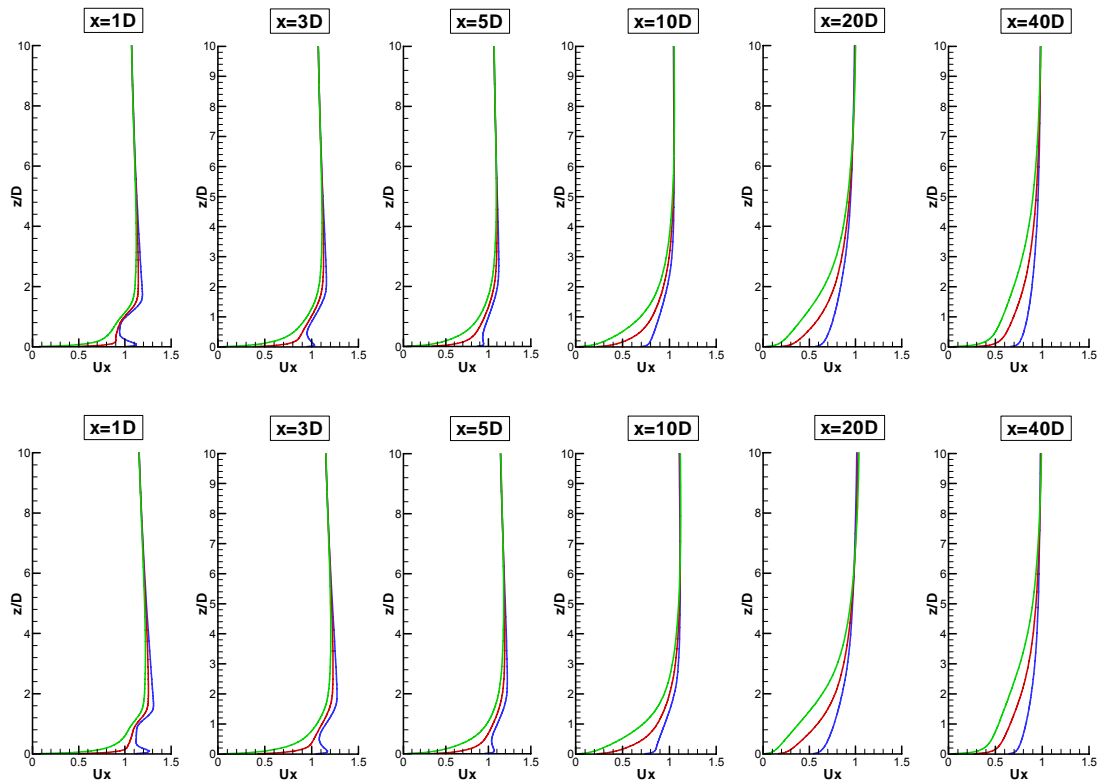


Figure 23: Vertical profiles of the streamwise wind speed downstream of the hill top in the presence of a W/T for various values of Tl_{in} : — 5%, — 13%, — 20%. Upper: 3D axisymmetric hill. Lower: Quasi-3D hill (wind direction 0°).

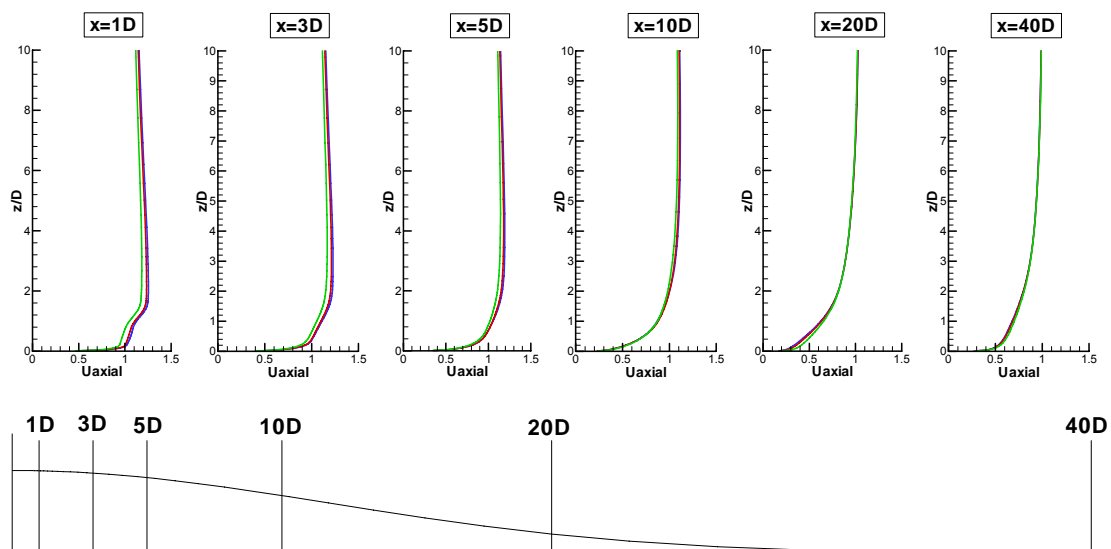


Figure 24: Vertical profiles of the turbulence intensity downstream the hill top of the quasi-3D hill for various wind directions: — 0° , — 15° , — 30° . Tl_{in} is 13%.

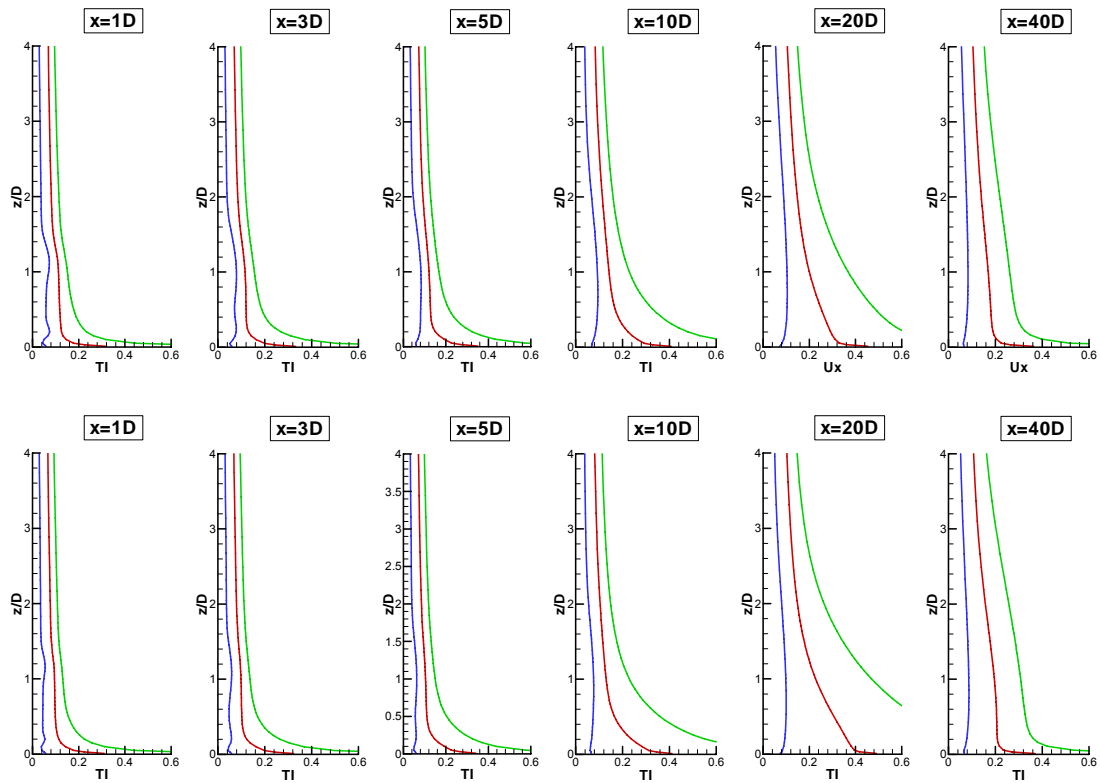


Figure 25: Vertical profiles of the turbulence intensity downstream the hill top in the presence of a W/T for various values of TI_{in} : — 5%, — 13%, — 20%.
Upper: 3D axisymmetric hill. Lower: Quasi-3D hill (wind direction 0°).

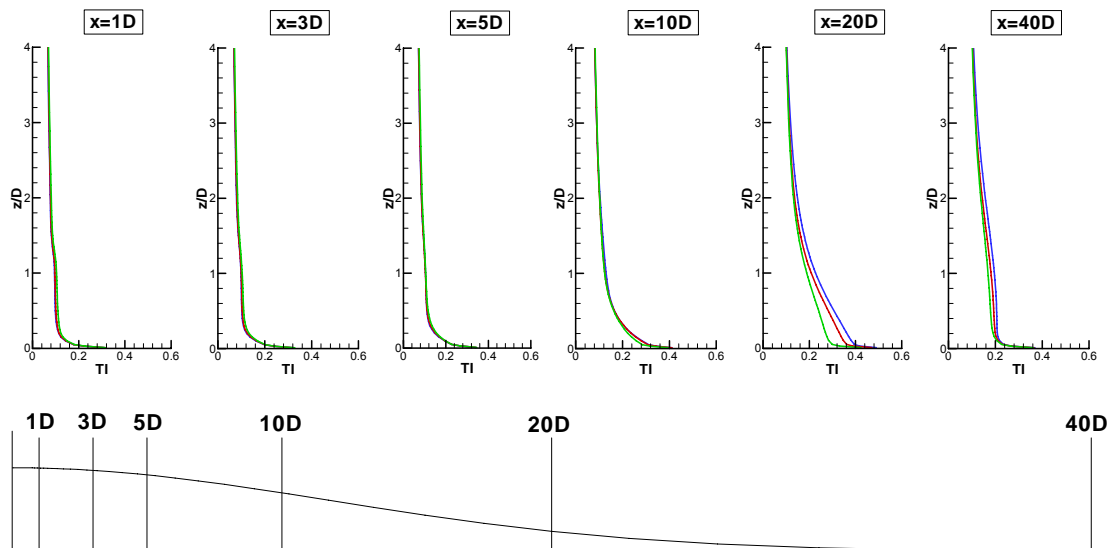


Figure 26: Vertical profiles of the turbulence intensity downstream the hill top of the quasi-3D hill for various wind directions: — 0° , — 15° , — 30° . TI_{in} is 13%.

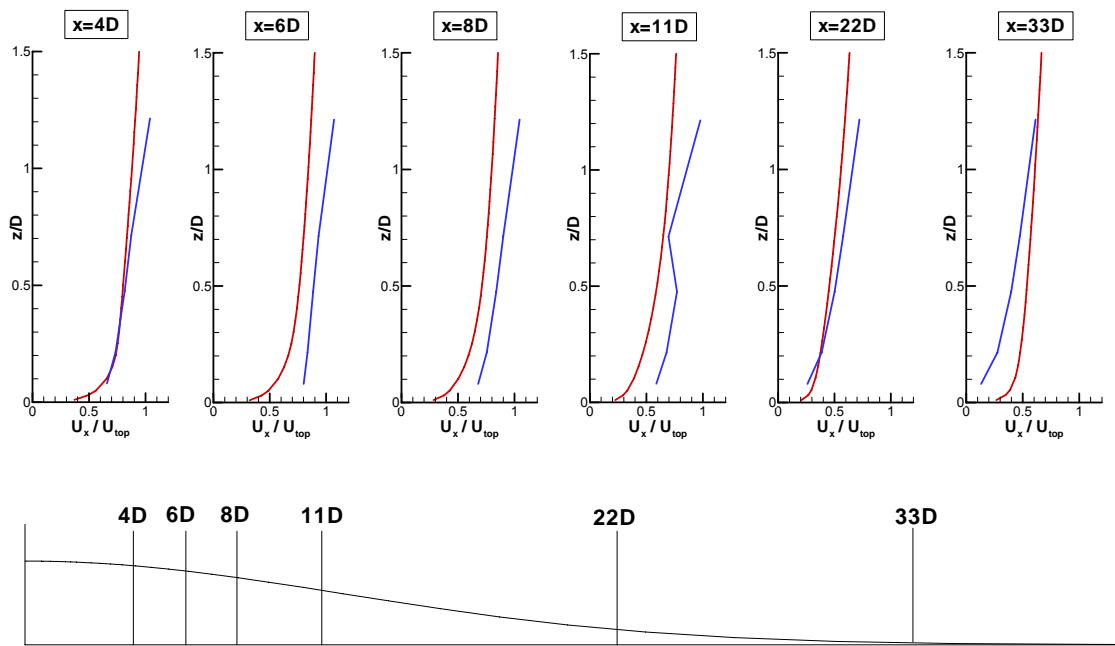


Figure 27: Vertical profiles of the streamwise velocity downstream the hill top of the 3D axisymmetric hill for various distances. — UEDIN (WAsP), — CRES (N-S). Tl_{in} is 13%. Normalization has been done with the predicted velocity at the hill top (hub height).

4.2.3 Wind speed contours

In Figure 28 the streamwise wind speed contours at the symmetry plane ($y = 0$) are plotted and compared between the axisymmetric and the quasi-3D hill. The discontinuity of the contours in the W/T region depicts the fact that the disk rotor operates as a momentum sink. This discontinuity is more pronounced for $Tl_{in} = 5\%$ and weakens as Tl_{in} increases, in agreement with the observations made in the streamwise variations and the wind speed profiles. This effect is more clearly represented in the wind speed contours at hub height a. g. l. (see Figure 29). In these contours, it can also be observed that the effect of the W/T presence is visible at long distances (more than $30D$) downstream the W/T.

In Figure 30, the streamwise wind speed contours are plotted at the transversal plane at $1D$ from the W/T for the two hill cases and for the various values of the inlet turbulence intensity studied. A scale-up has been made in the region of the disk rotor, the perimeter of which is drawn along with the computational grid. For $Tl_{in} = 5\%$ a stronger effect of the rotor disk in the wake is observed, which is in agreement with the abrupt wind speed drop observed in Figure 21a and the wind speed profiles shown in Figure 23. In both hill cases, the wake centre is below the disk rotor centre. As the level of Tl_{in} increases, the W/T effect on the wake diminishes, as also observed in the wind speed profiles. Finally, the wind speed contours for the total horizontal wind speed $U_{tot} = \sqrt{U_x^2 + U_y^2}$ at hub height a. g. l. are presented in Figure 31 for the wind directions of 15° and 30° . The lower accelerations and decelerations predicted for the 30° wind direction case are due to the fact that the flow follows a relatively smoother terrain. Figure 31 also shows that the wind speed deficit occurs in the direction of the flow at the rotor centre which is 10° and 20° , respectively, as the disk rotor has been rotated during the generation of the grid by an equal yaw angle, so that its surface remains perpendicular to the flow.

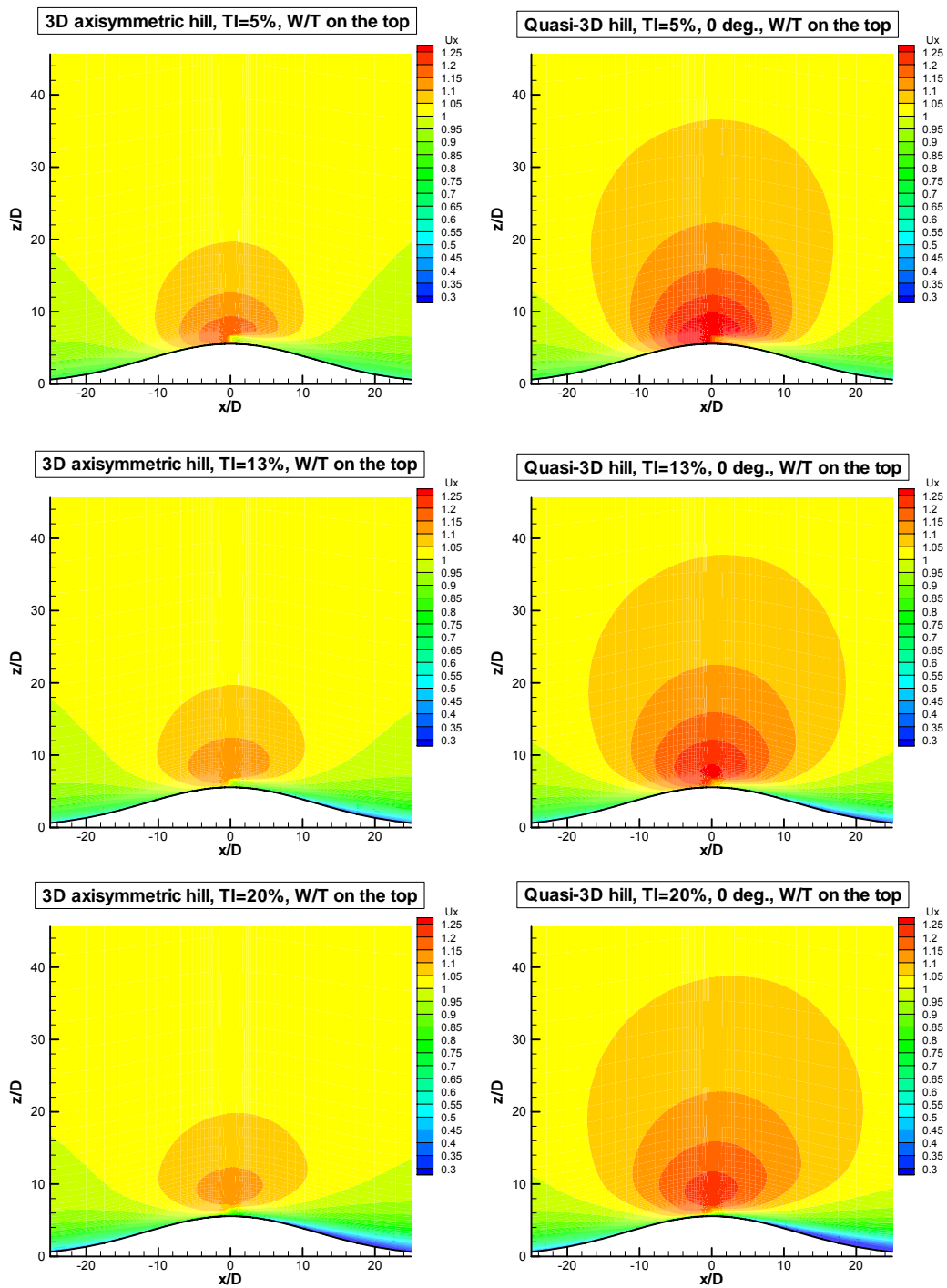


Figure 28: Streamwise wind speed contours for the axisymmetric and quasi-3D hill at the symmetry plane ($y = 0$). Upper: $TI_{in} = 5\%$. Middle: $TI_{in} = 13\%$. Lower: $TI_{in} = 20\%$.

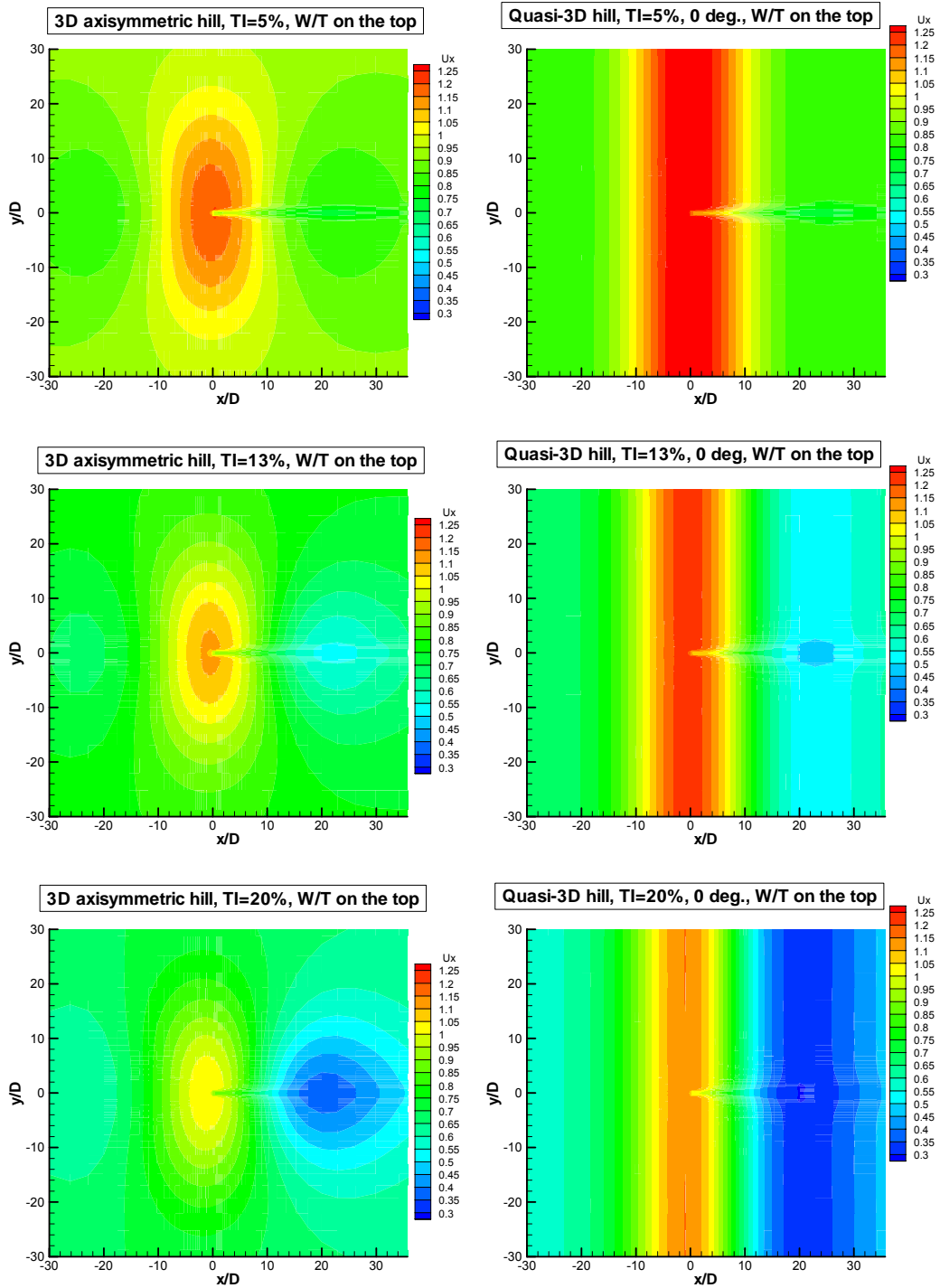


Figure 29: Streamwise wind speed contours for the axisymmetric and quasi-3D hill at hub height $a. g. l.$ Upper: $TI_{in} = 5\%$. Middle: $TI_{in} = 13\%$. Lower: $TI_{in} = 20\%$.

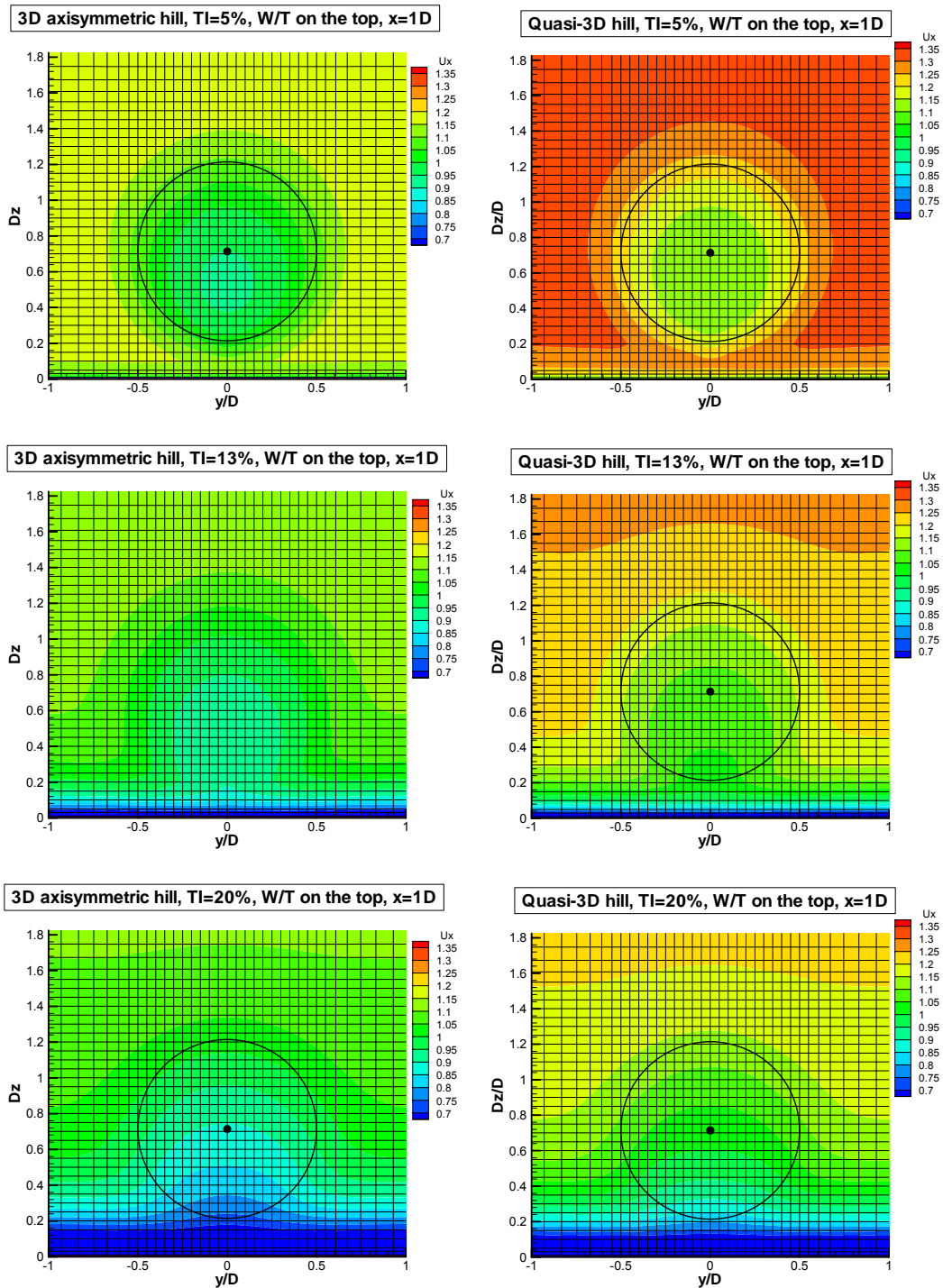


Figure 30: Streamwise wind speed contours for the axisymmetric and quasi-3D hill at plane $x = 1D$ downstream the W/T. Upper: $TI_{in} = 5\%$. Middle: $TI_{in} = 13\%$. Lower: $TI_{in} = 20\%$.

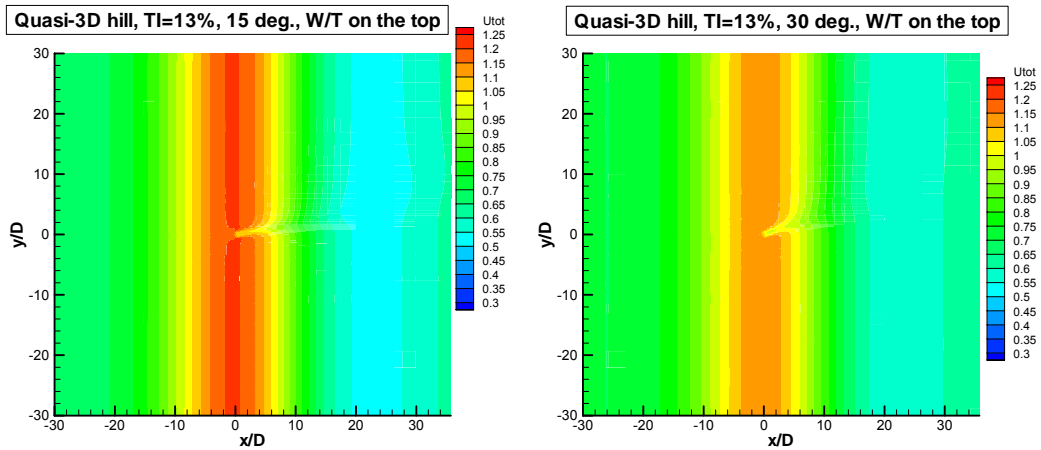


Figure 31: Streamwise wind speed contours above the quasi-3D hill at hub height a. g. l. for wind directions of 15° and 30° for $TI_{in} = 13\%$.

4.3 Wind speed deficit prediction

The wind speed deficit ΔU in the presence of a wind turbine is calculated with reference to the flow field without W/T, using the relationship:

$$\Delta U = \frac{DU_x}{U_{ref} \times C_t} = \frac{U_{axial}(\text{without } W/T) - U_{axial}(\text{with } W/T)}{U_{axial}(\text{without } W/T) \times C_t}.$$

In the above definition, U_{axial} is the U_x wind speed for 0° wind direction or the total horizontal wind speed $U_{tot} = \sqrt{U_x^2 + U_y^2}$ when the wind direction is 15° or 30° .

4.3.1 Deficit at hub height

In Figure 32, the wind speed deficit is presented for the 3D axisymmetric hill, the quasi-3D hill and the flat terrain case for different levels of TI_{in} . One important conclusion is that in both hill cases the deficit remains significant at long distances (even greater than $40D$) downstream the W/T. On the contrary, in the flat terrain case, the deficit is already practically negligible at $20D$. The decay rate is even slower for the quasi-3D hill. The comparison between hill and flat terrain cases is better shown in Figure 36. The increase of the turbulence level results in a faster flow recovery at long distances as expected. However, it is noticeable that the wind speed deficit at hub height is not always monotonously decreasing. This is mainly observed in the quasi-3D case and is more pronounced for the $TI_{in} = 20\%$ case (Figure 32b, Figure 36).

The wind speed deficit predictions between CRES and CENER are compared in Figure 33. The reference C_t used for the calculation of the disk rotor force is higher in the CENER predictions, indicating that lower velocities have been predicted in the case without W/T. For $TI_{in} = 5\%$, CRES and CENER calculated $C_t = 0.39$ and 0.383 respectively, whereas for $TI_{in} = 13\%$ the respective values are 0.317 and 0.27 . CRES predicts a faster decay rate which is a result of the higher C_t predicted value or equivalently of the lower predicted velocity at the hill top. The comparison of wind speed deficit predictions between CRES, CENER and UEDIN is presented in Figure 34. UEDIN predicts a slower wind speed deficit decay in the far wake, especially for $TI_{in} = 13\%$ and $TI_{in} = 20\%$, than the two Navier–Stokes codes. For $TI_{in} = 5\%$ and $TI_{in} = 20\%$ a close agreement is observed between CRES and UEDIN up to the distance of $10D$. However, at that distance UEDIN predicts a rather peculiar increase in the deficit, which leads to divergence of the predictions at longer distances. Regarding the turbulence intensity

predictions (Figure 35), the agreement between CRES and CENER is very good for $TI_{in} = 13\%$, whereas small differences are observed in the wake region for the $TI_{in} = 5\%$ case.

Another important remark is the drastic effect of the wind direction on the decay rate of deficit. In Figure 37, it is observed that the change of the wind direction from 0° to 30° significantly increases the decay rate. At 30° wind direction, the decay rate of deficit is comparable to that of flat terrain.

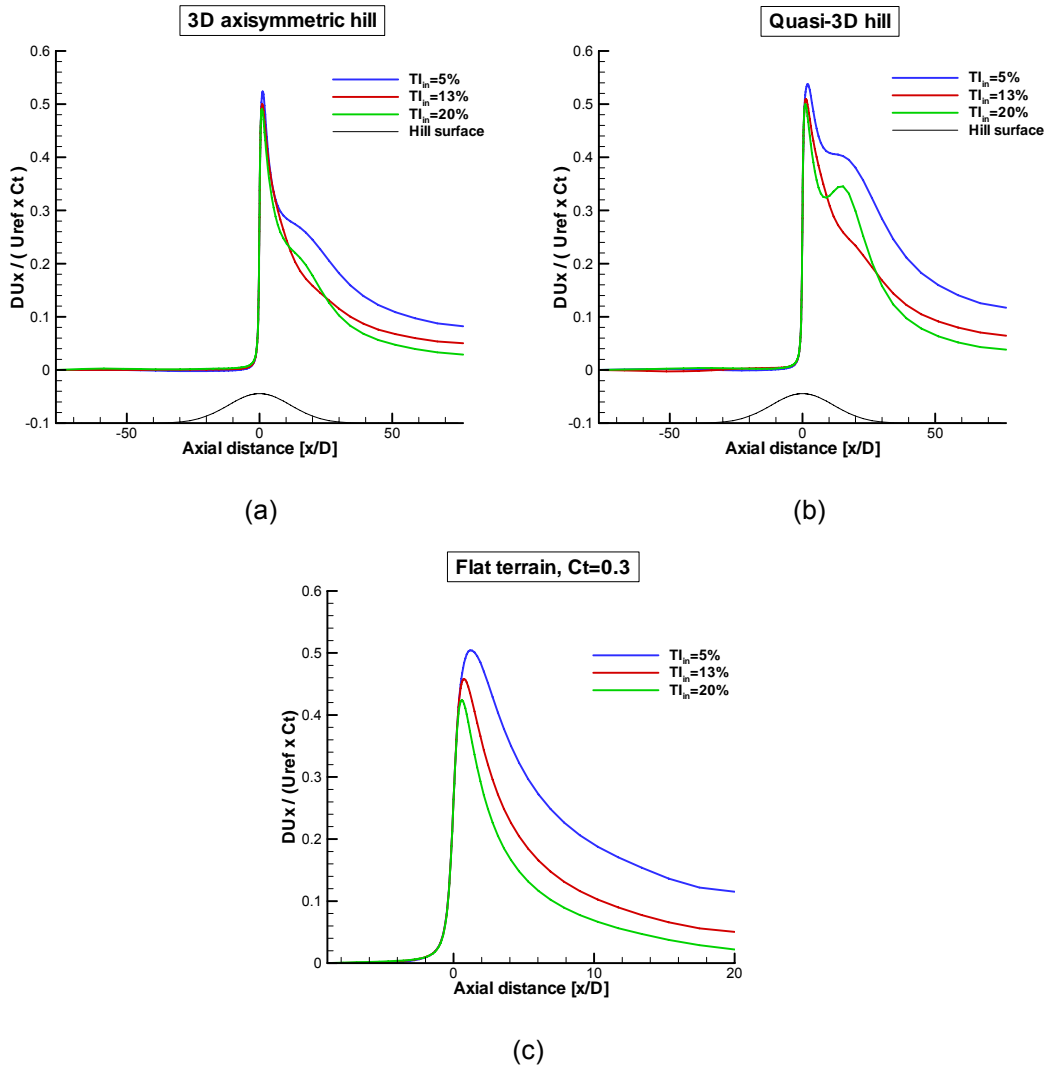


Figure 32: Wind speed deficit along $y = 0$ line at hub height a. g. l. for various values of TI_{in} . (a) axisymmetric hill, (b) quasi-3D and (c) flat terrain. Wind direction is 0° .

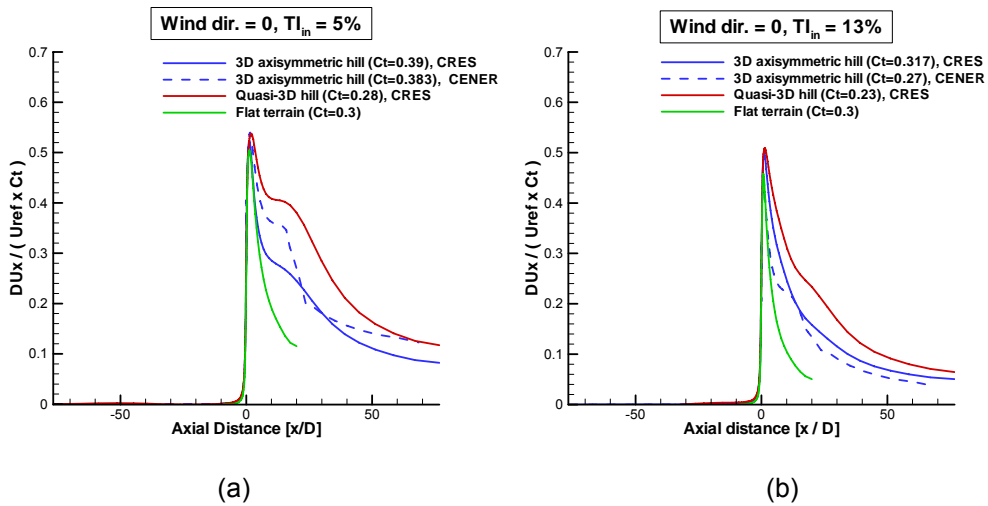


Figure 33: Wind speed deficit for (a) $TI_{in} = 5\%$ and (b) $TI_{in} = 13\%$.

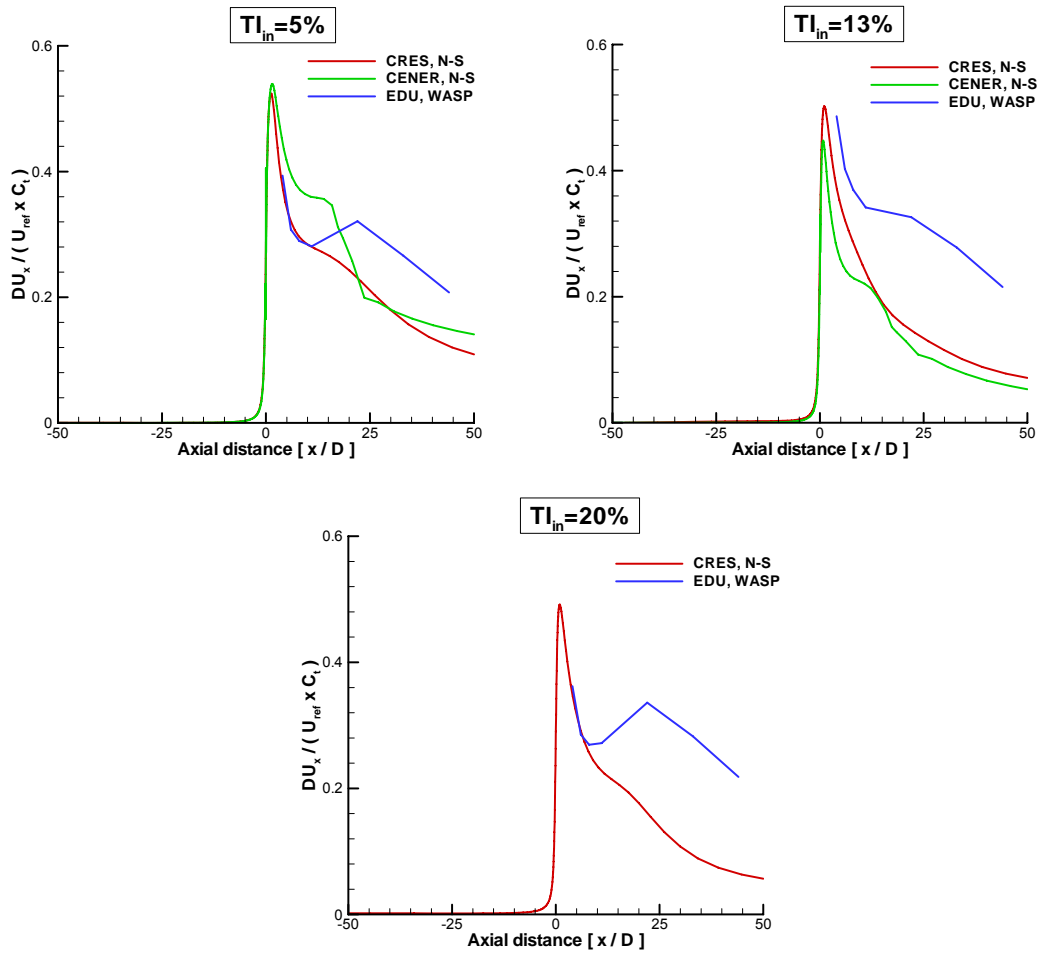


Figure 34: Wind speed deficit for (a) $TI_{in} = 5\%$, (b) $TI_{in} = 13\%$ and (b) $TI_{in} = 20\%$. Comparison between CRES (N-S), CENER (N-S) and UEDIN (WASP).

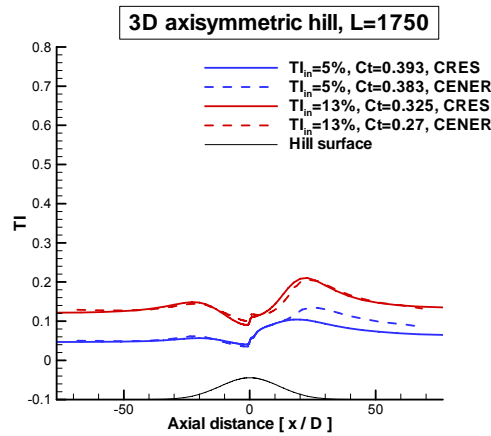


Figure 35: Turbulence intensity along $y = 0$ line at hub height a. g. l. for TI_{in} 5% and 13%.

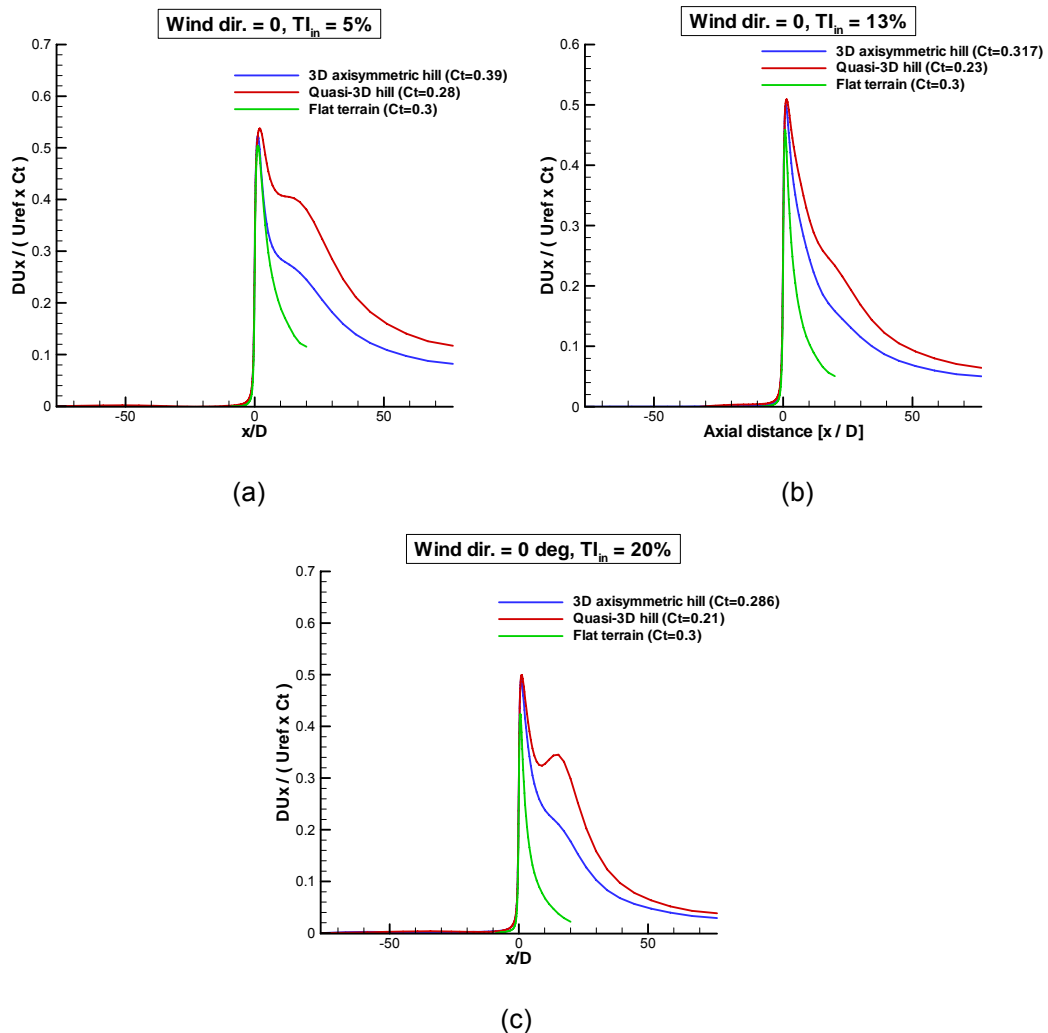


Figure 36: Wind speed deficit at the hub height a. g. l. for axisymmetric hill, quasi-3D hill and flat terrain. TI_{in} is (a) 5%, (b) 13% and (c) 20%. Wind direction is 0° .

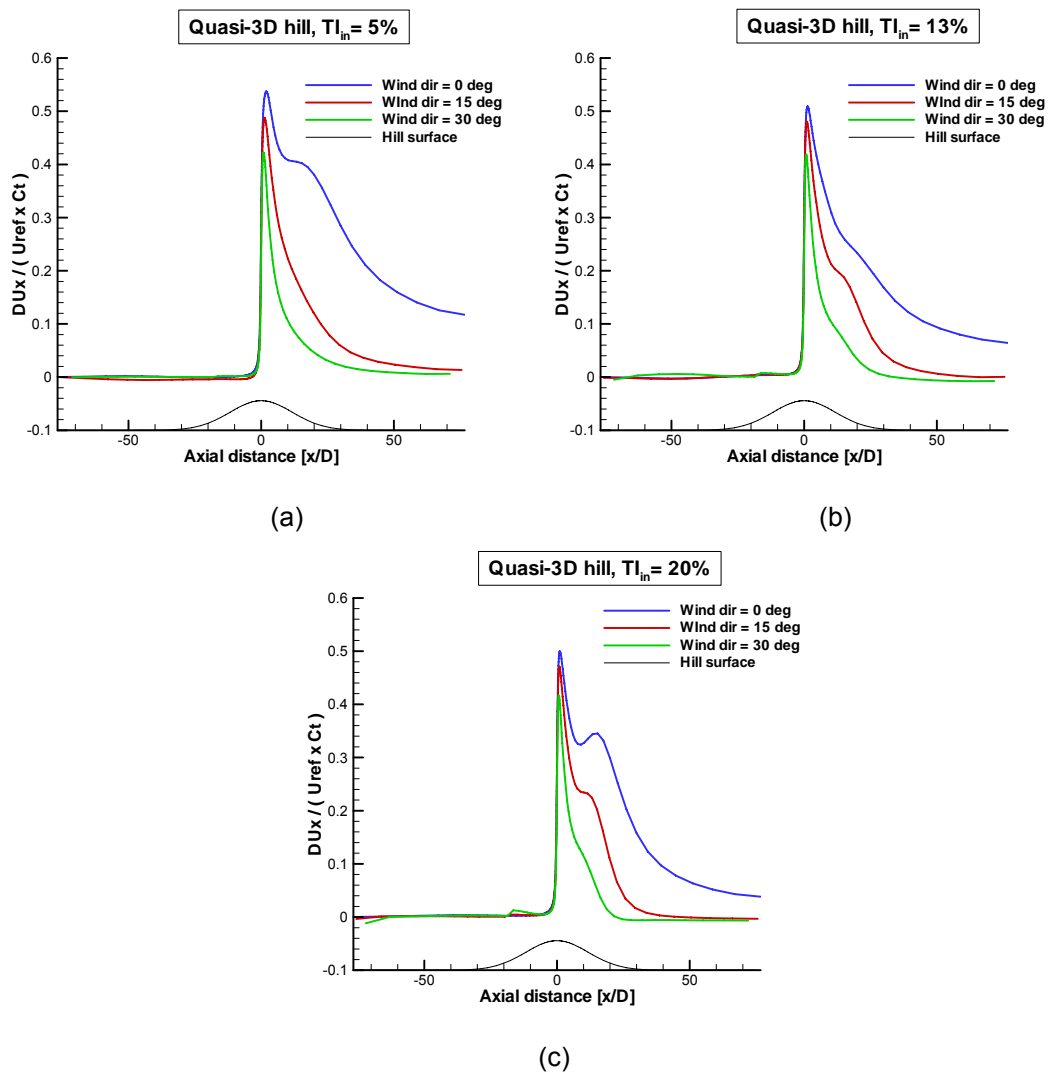


Figure 37: Wind speed deficit at hub height along the W/T orientation for quasi-3D hill and various wind directions. TI_{in} is: (a) 5%, (b) 13% and (c) 20%.

4.3.2 Vertical profiles

In Figure 38 the vertical deficit profiles are plotted at increasing distance downstream the hill top. A straightforward observation is the modification of the wake geometry with turbulence, especially in the $TI_{in} = 20\%$ case, which is responsible for the aforementioned non-monotonous variation of the deficit in the stream-wise direction. The height of the maximum deficit reduces with increasing TI_{in} and for $TI_{in} = 20\%$ is located close to the ground. Another remark is that the predicted deficit maintains higher values in the quasi-3D hill case, denoting a slower decay rate, which was also seen in the stream-wise variations. The deficit values remain significant after $20D$ and in some cases even after $40D$ ($TI_{in} = 5\%$).

The significant effect of the wind direction on the deficit is confirmed by the profiles shown in Figure 39. The height of the maximum deficit remains constant denoting similar wake geometry; its level, however, attenuates fast as the wind direction changes from 0 to 30° . For the latter case, the wind speed deficit is practically negligible after $20D$.

In Figure 40, the deficit profiles for the axisymmetric and the quasi-3D hill cases are compared with those predicted in the flat terrain case. The increase of deficit in level and size, as well as its slower decay rate for the hill cases are clearly shown. In the flat terrain case, the position of

maximum deficit remains almost constant, a little lower than hub height. In both hill cases, the position of maximum deficit moves downwards up to a certain distance which depends on the inlet level of turbulence, and then it is gradually elevated until the wake vanishes.

In Figure 41, the comparison of the predicted velocity deficit and turbulence intensity profiles between CRES and CENER is presented. The agreement between the turbulence intensity profiles is good, with the exception of small heights for the $TI_{in} = 5\%$ case, at which CENER predicts higher values. This difference, which could be attributed to the wall function treatment on the ground, could be responsible for the higher velocity deficit predicted by CENER at all positions up to $20D$ distance. For the $TI_{in} = 13\%$ case, CENER predicts slightly lower velocity deficit at the same positions. The overall good agreement on the TI predictions indicates that the velocity deficit difference is not caused from the different turbulence models, $k-\omega$ (CRES) and $k-\epsilon$ (CENER).

The large differences in wind speed deficit between Navier–Stokes and WAsP predictions is also depicted in the vertical profiles of Figure 42. The comparison of the profiles at distances greater than $11D$ shows that the WAsP predictions retain higher deficit values in the far wake.

4.3.3 Deficit contours

In Figure 43 and Figure 44 the deficit contours at the plane $y = 0$ are compared for the two hills and the flat terrain case. The wake evolution at long distances in both hill cases, and particularly in the quasi-3D case, contrasts the quick vanishing in the flat terrain case. It also clearly depicts that the increase of TI_{in} favours a faster wake deficit attenuation.

Similar remarks can be made by observing the contour plots at constant hub height a. g. l. in Figure 45 and Figure 46. In this plane, however, a wider spreading of the wake is also visible as the turbulence level increases. A more detailed illustration of the wake geometry can be made by focusing on the region behind the W/T at a plane parallel to the rotor disk. In Figure 47, Figure 48 and Figure 49 the deficit contours are presented at $1D$ and $5D$ downstream the W/T for various TI_{in} values (5%, 13% and 20%). In the flat terrain case, the wake centre is located about $0.05D$ lower than hub height at $1D$ downstream. This height difference becomes about $0.1D$ at $5D$ downstream. In the axisymmetric and the quasi-3D hill cases, the height difference between wake centre and hub is about $0.15D$ at $1D$ downstream and becomes about $0.2D$ at $5D$ downstream. In Figure 47b, it seems that for the $TI_{in} = 20\%$ case, the circular shape of the wake geometry has already been distorted at $5D$ downstream. Finally, the effect of wind direction on the wake geometry is shown in Figure 50. As the wind direction changes from 0 to 30° , a faster attenuation and a wider spreading of the wake occurs.

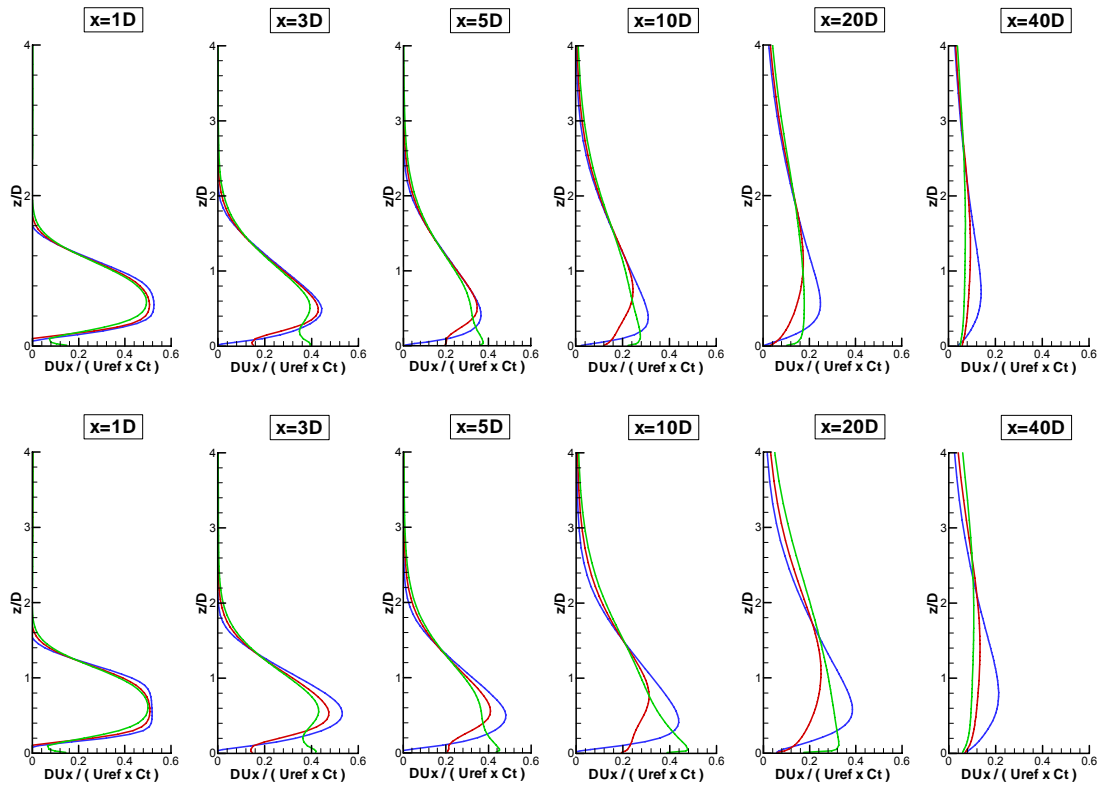


Figure 38: Quasi-3D hill – Vertical profiles of wind speed deficit downstream the hill top in the presence of W/T for axisymmetric (upper) and quasi-3D (lower) hills and various values of TI_{in} :
— 5%, — 13%, — 20%.

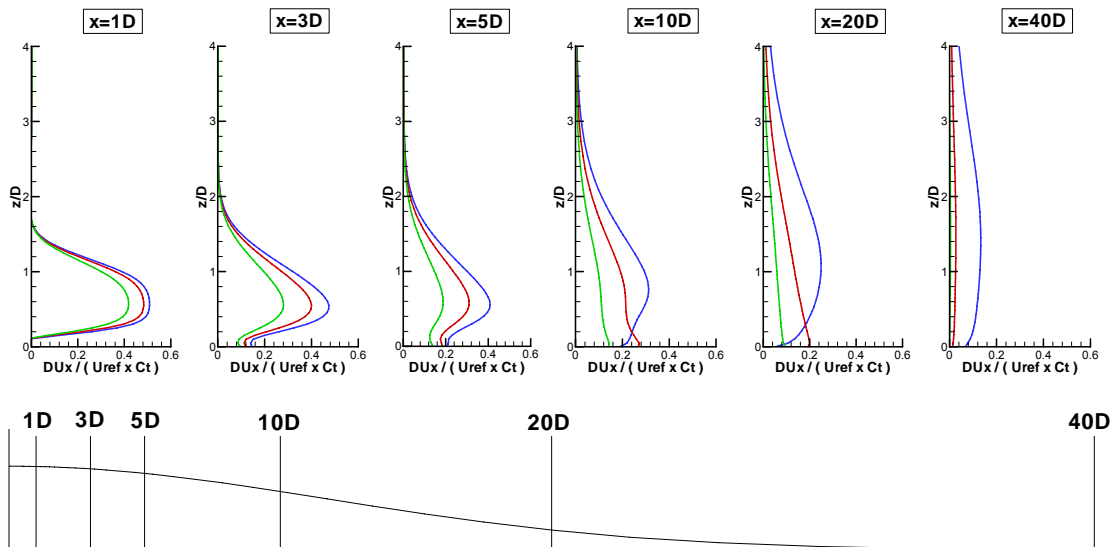


Figure 39: Quasi-3D hill – Vertical profiles of wind speed deficit downstream the hill top in the presence of W/T for various wind directions: — 0° , — 15° , — 30° . $TI_{in} = 13\%$.

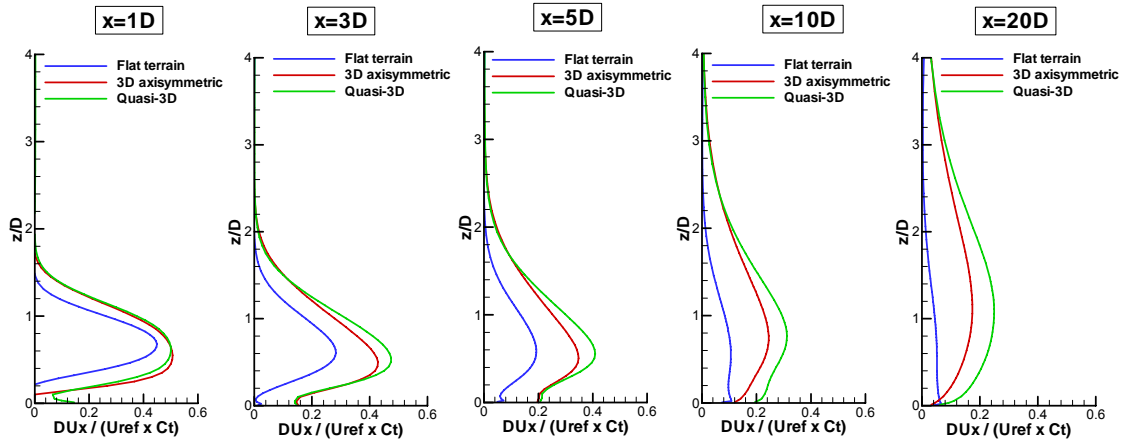


Figure 40: Comparison of wind speed deficit vertical profiles among 3D axisymmetric hill, quasi-3D hill and flat terrain at increasing distance downstream the W/T. $Tl_{in} = 13\%$

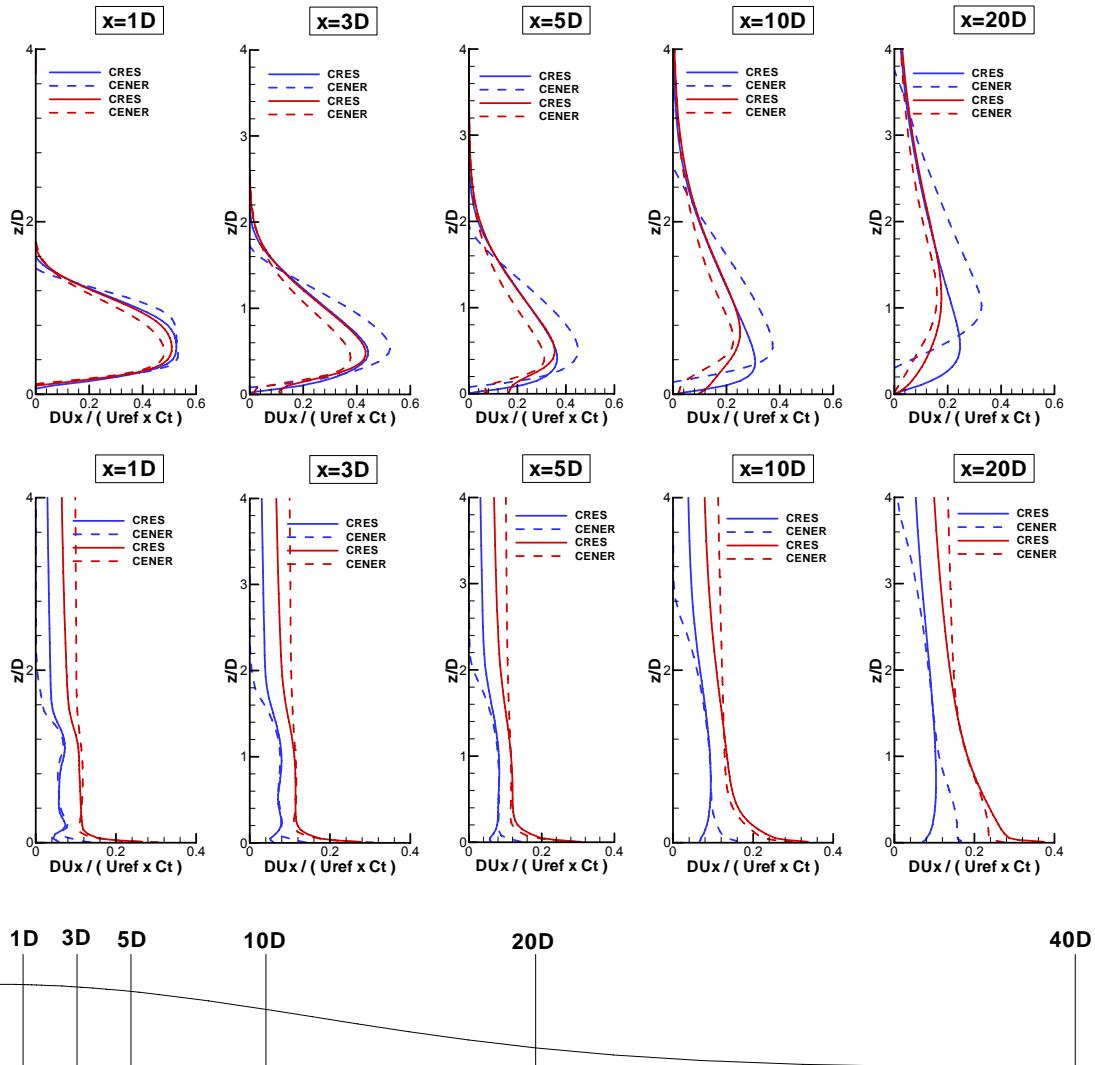


Figure 41: Comparison of wind speed deficit and turbulence intensity vertical profiles between CRES and CENER at increasing distance downstream the W/T. Tl_{in} : — 5%, — 13%

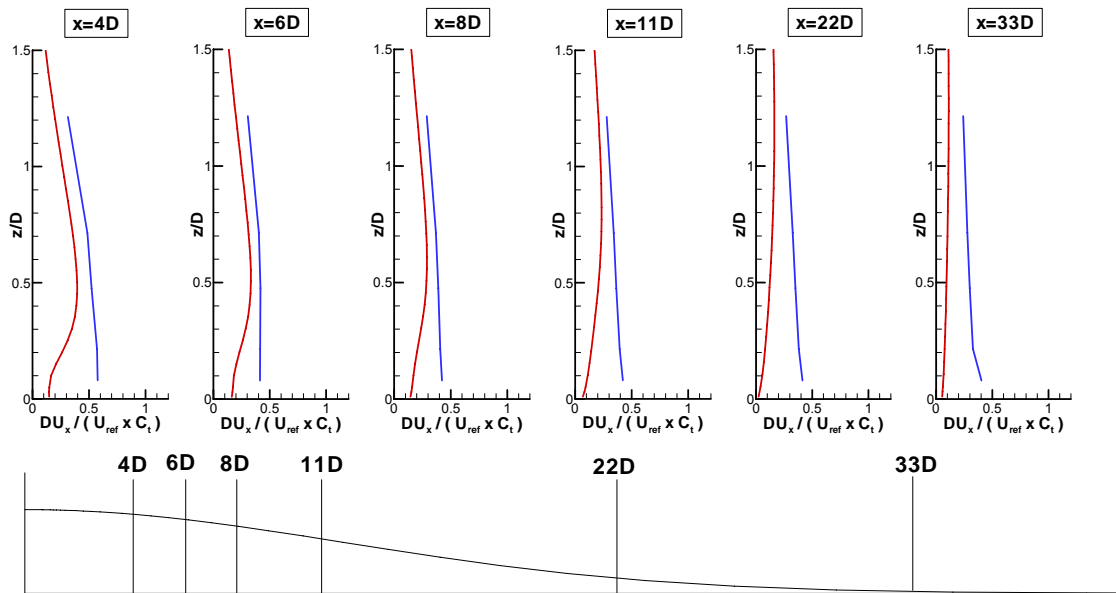


Figure 42: Comparison of wind speed deficit vertical profiles between CRES (N-S) — and UEDIN (WasP) — at increasing distance downstream the W/T. Ti_{in} is 13%.

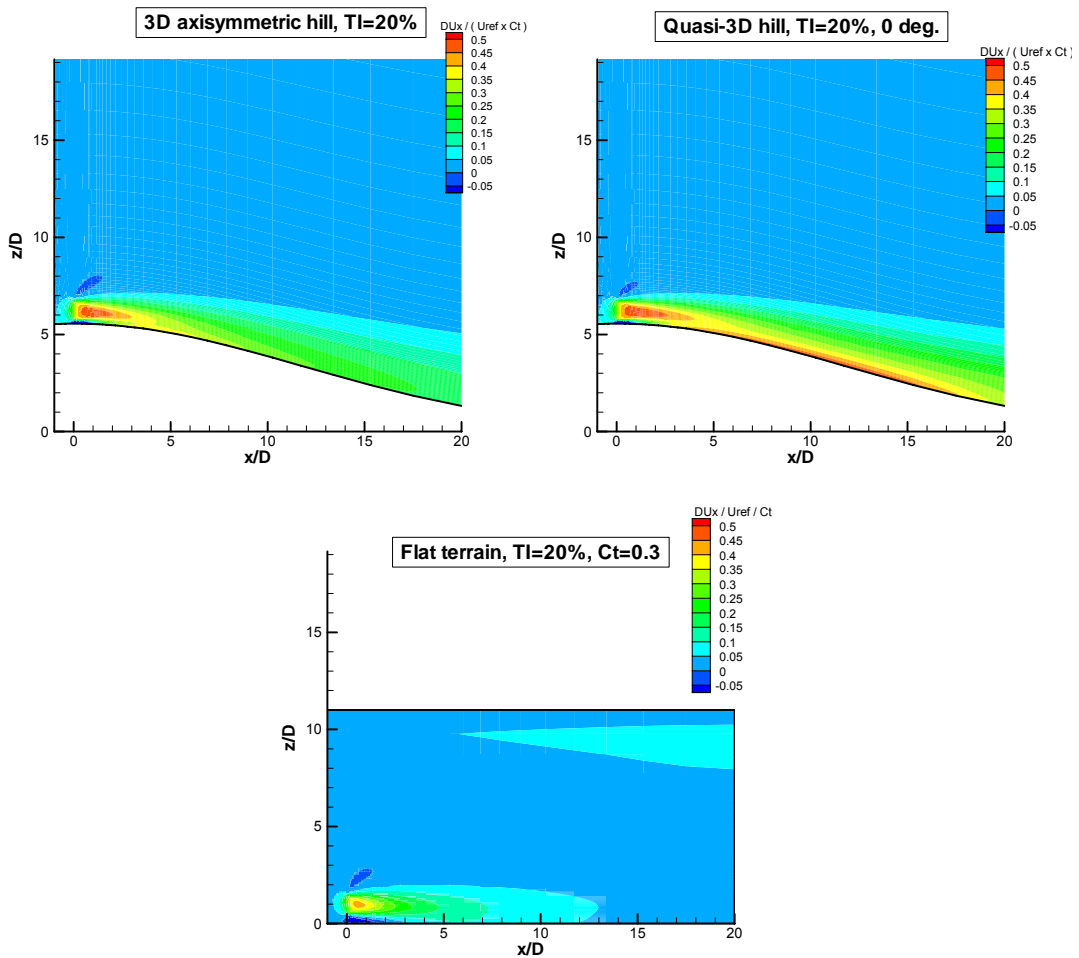


Figure 43: Comparison of wind speed deficit contours at the symmetry plane ($y = 0$) among flat terrain, 3D axisymmetric hill and quasi-3D hill. $Ti_{in} = 20\%$.

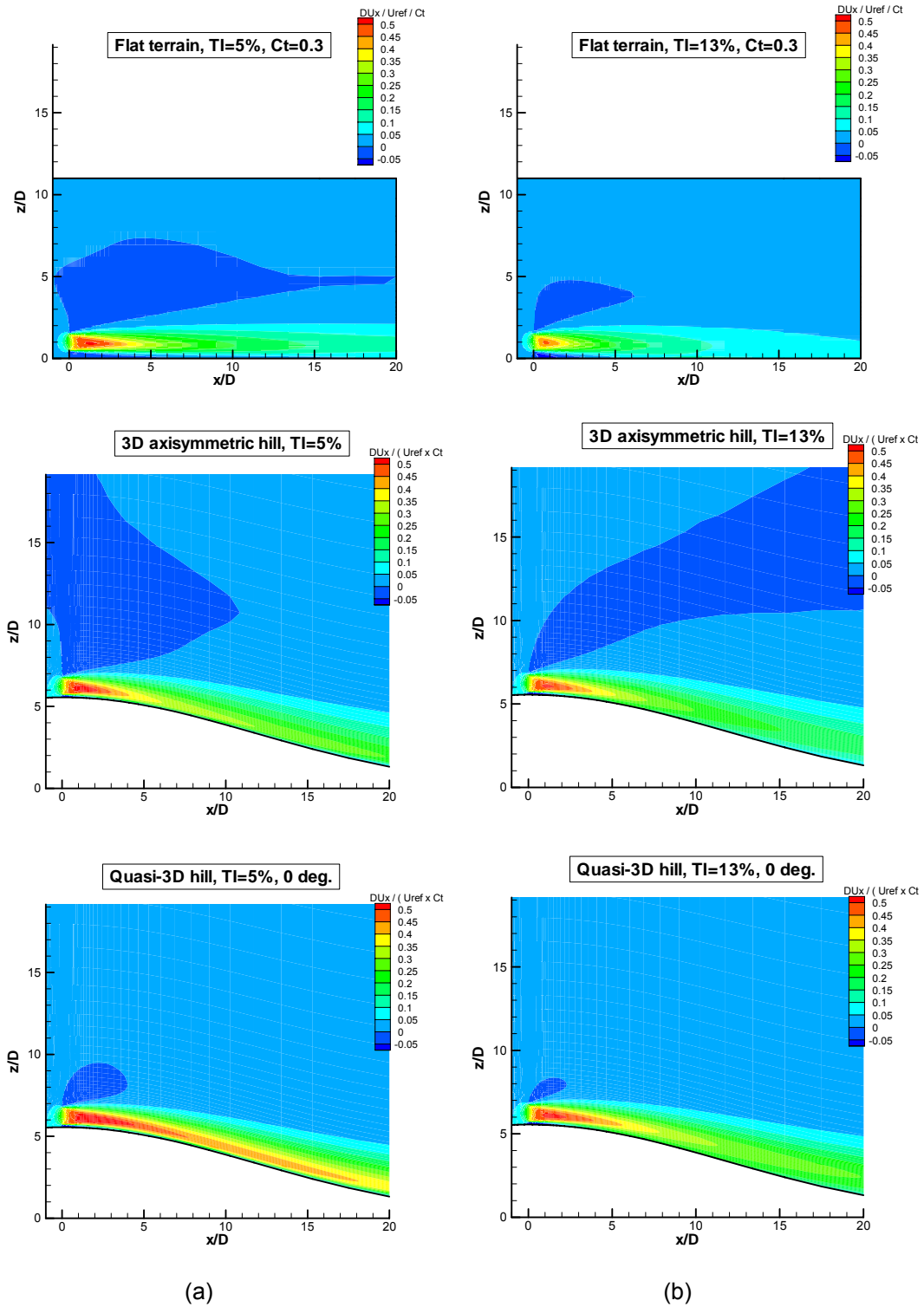


Figure 44: Comparison of wind speed deficit contours at the symmetry plane ($y = 0$) among flat terrain, 3D axisymmetric and quasi-3D hill. TI_{in} is (a) 5% and (b) 13%.

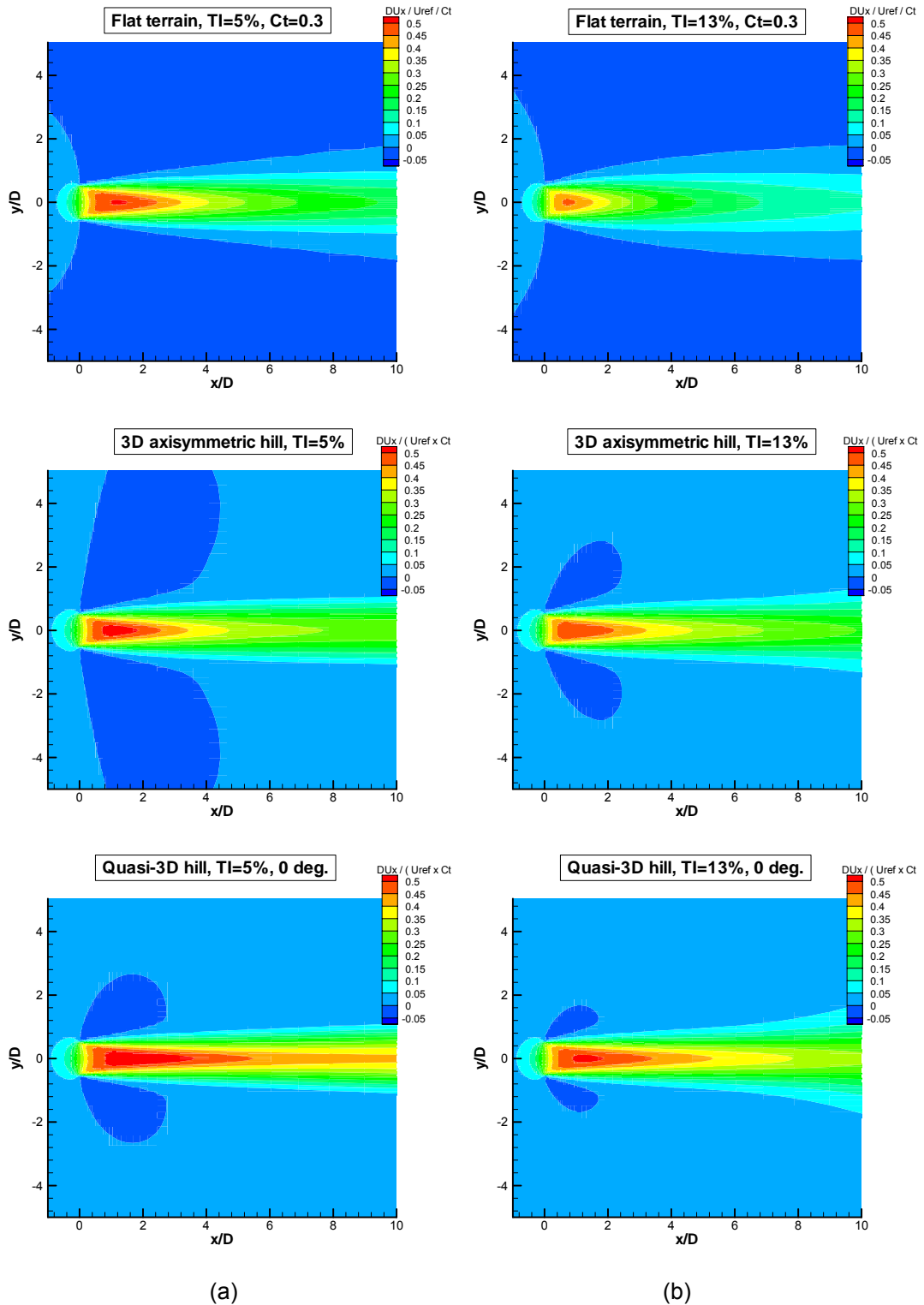


Figure 45: Comparison of wind speed deficit contours at hub height a. g. l. among flat terrain, 3D axisymmetric hill and quasi-3D hill. TI_{in} is (a) 5% and (b) 13%.

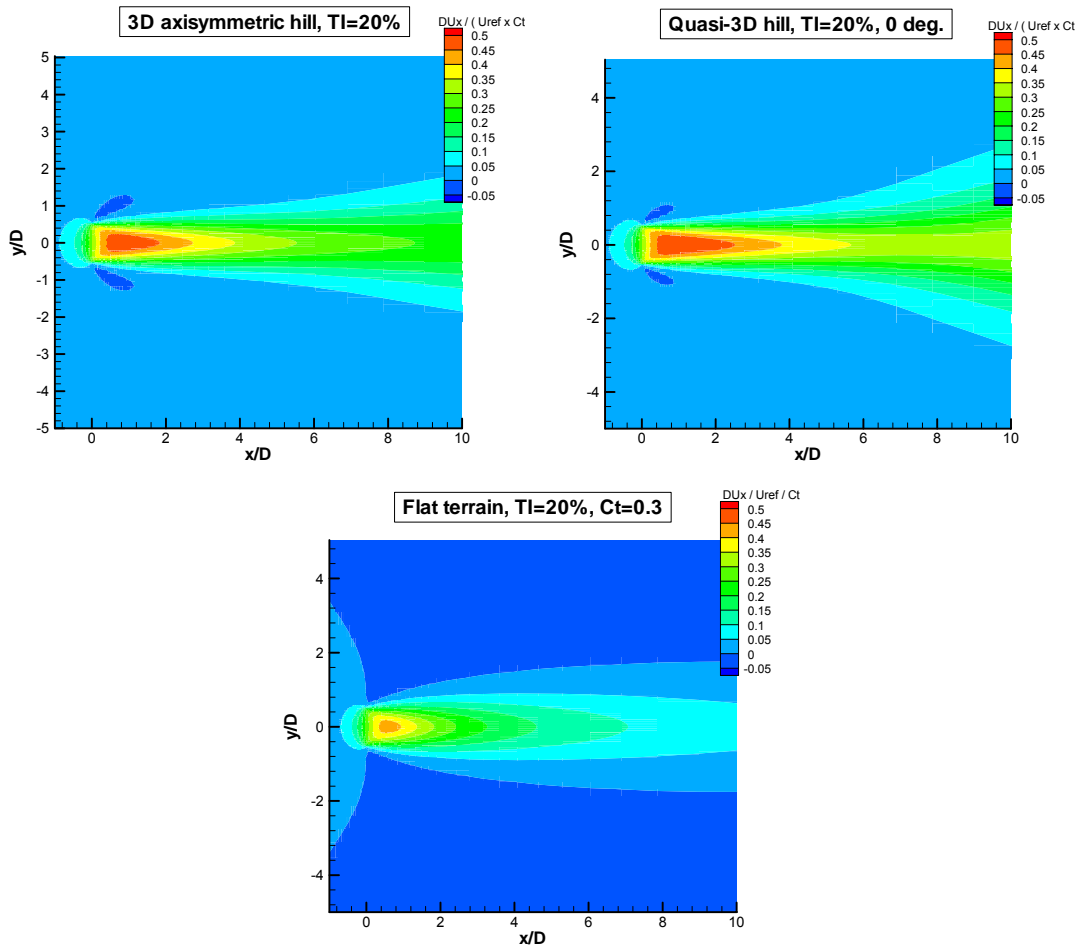


Figure 46: Comparison of wind speed deficit contours at hub height a. g. l. among flat terrain, 3D axisymmetric hill and quasi-3D hill for $Tl_{in} = 20\%$.

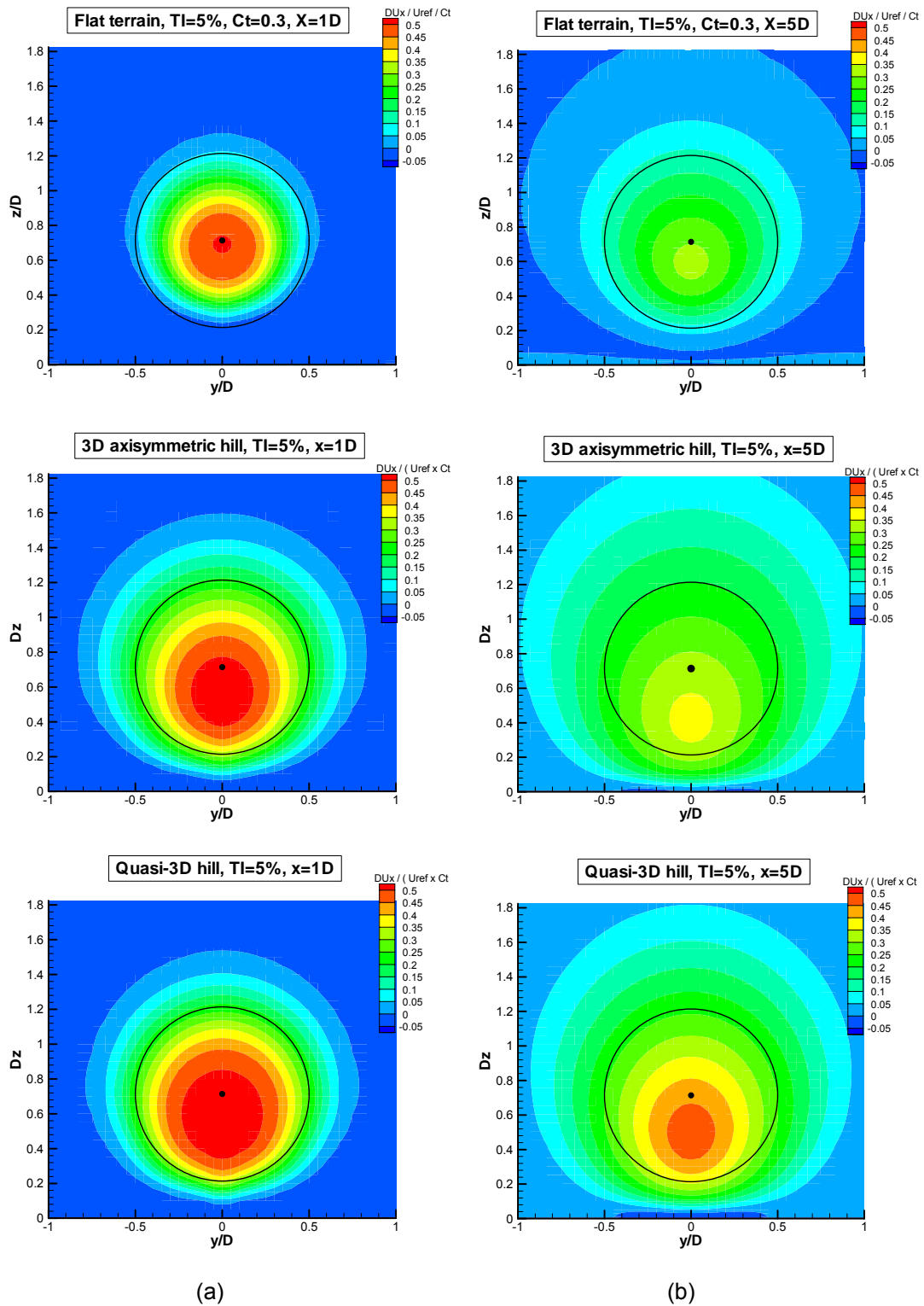


Figure 47: Comparison of wind speed deficit contours at (a) $x = 1D$ and (b) $x = 5D$ downstream the hill top among flat terrain, 3D axisymmetric hill and quasi-3D hill. $TI_{in} = 5\%$.

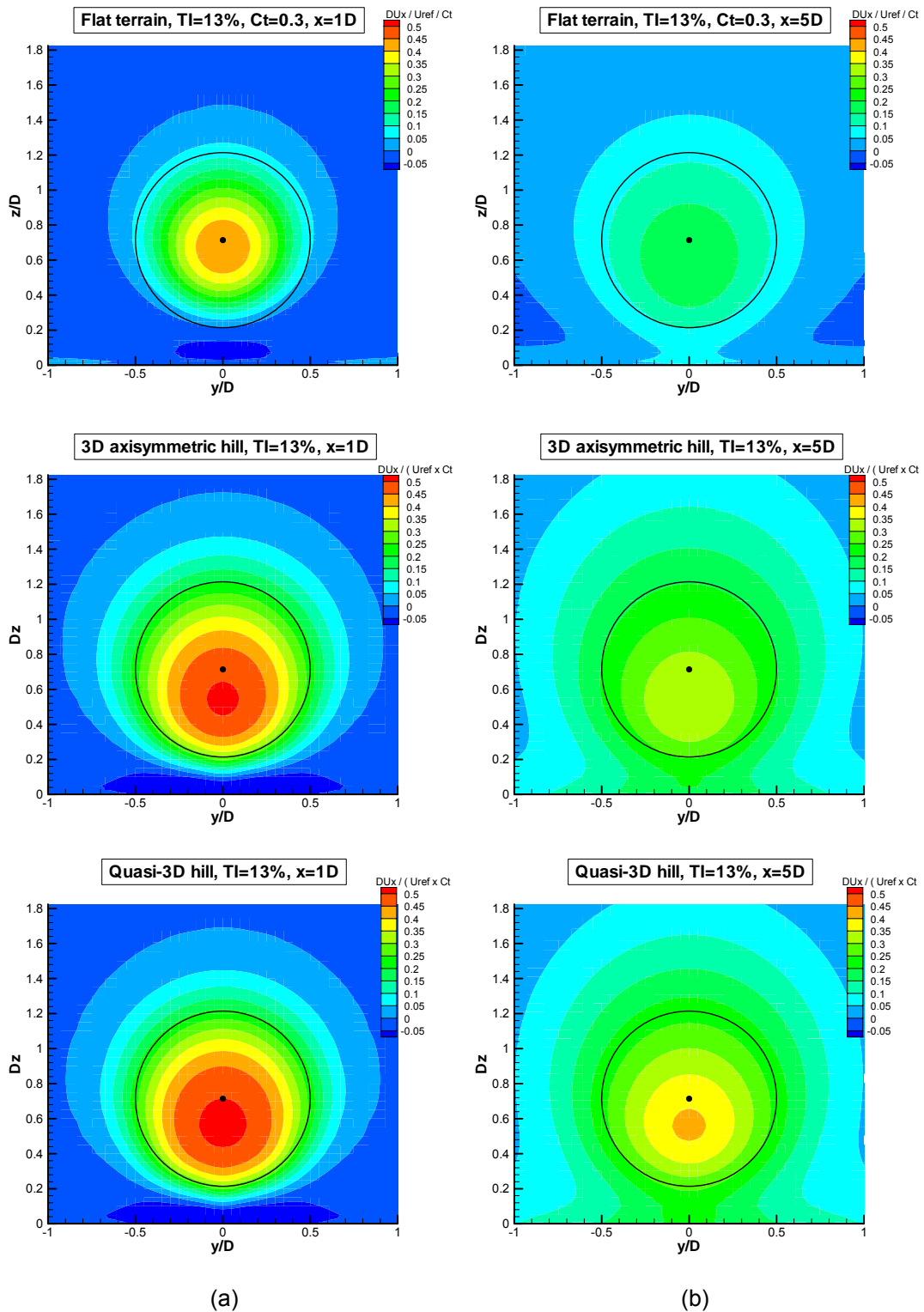


Figure 48: Comparison of wind speed deficit contours at (a) $x = 1D$ and (b) $x = 5D$ downstream the W/T among flat terrain, 3D axisymmetric hill and quasi-3D hill. TI_{in} is 13%.

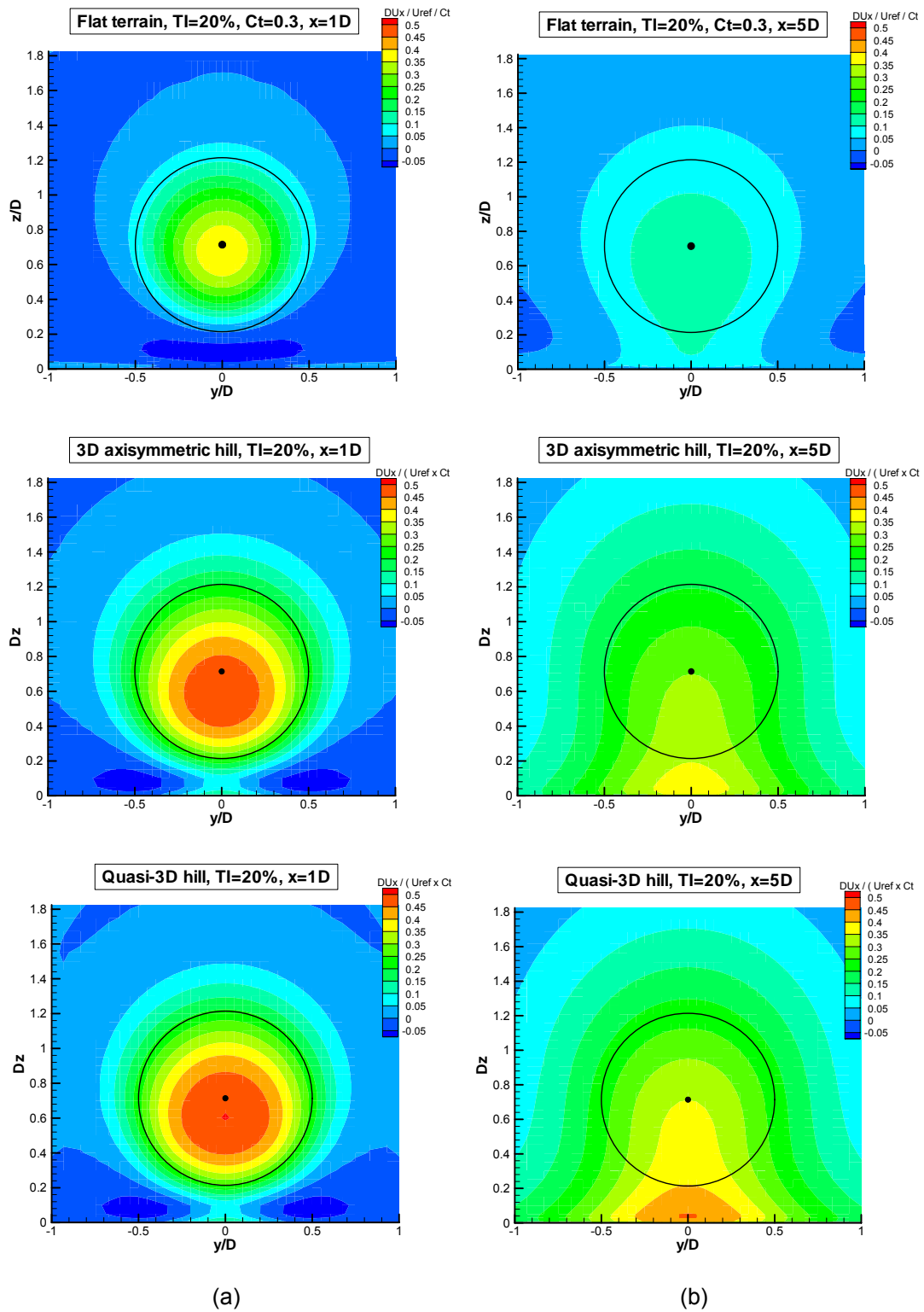


Figure 49: Comparison of wind speed deficit contours at (a) $x = 1D$ and (b) $x = 5D$ downstream the W/T among flat terrain, 3D axisymmetric hill and quasi-3D hill. $TI_{in} = 20\%$.

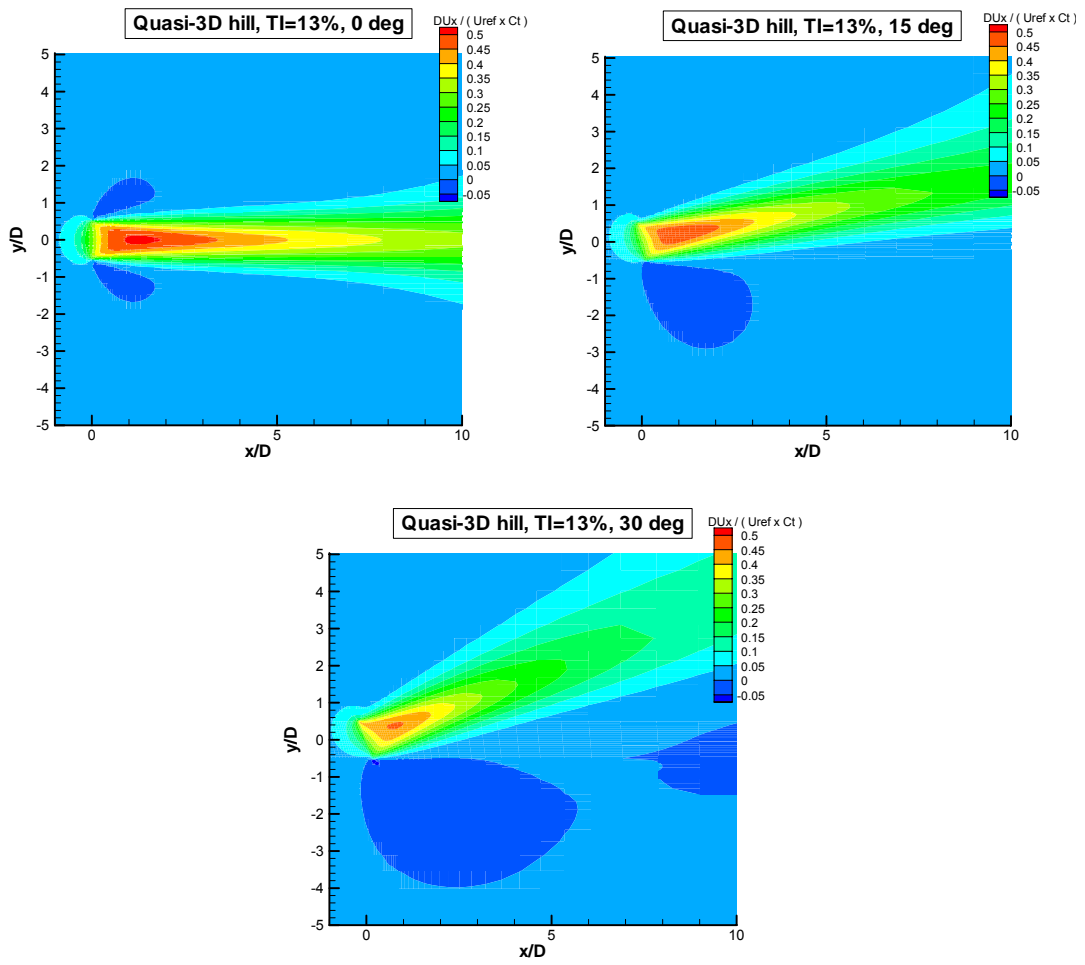


Figure 50: Wind speed deficit contours at hub height for quasi-3D hill for 0, 15 and 30° wind directions. Yaw angle is 0, 10 and 20°, respectively. $TI_{in} = 13\%$.

5. Conclusions

The wake characteristics of a paper case 5 MW wind turbine situated on the top of a Gaussian hill were investigated through a Navier–Stokes based analysis in this report and compared with the respective characteristics in flat terrain. Two different hill geometries were examined, a 3D axisymmetric and a quasi-3D one. The effects of the hill terrain, the turbulence intensity and the wind direction on the wake characteristics were assessed. For the sake of completeness, wind speed and turbulence intensity predictions were first presented for the reference cases without W/T. The basic conclusions drawn from the numerical analysis can be summarized below.

The change of the inlet turbulence intensity, which is equivalent to a change in roughness, affects the shape of the wind speed boundary layer. An increase in the inlet turbulence produces higher accelerations at the hill top and higher decelerations at the lee side of the hill. This effect is reinforced by the W/T presence and is more pronounced in the quasi-3D hill. As a result, the increase of the TI_{in} causes a decrease in the C_t value of the W/T, implying a weaker effect on the wind speed deficit.

The presence of the hill increases significantly the turbulence intensity downstream the W/T. The maximum values occur in the region of highest flow deceleration, about $20D$ downstream the W/T. In a flat terrain, any increase in turbulence is caused only by the W/T presence.

In both hill cases the deficit remains significant at $20D$ from the W/T, and in some cases even at $40D$ (for the lower turbulence intensity value examined, $TI_{in} = 5\%$). On the contrary, in the flat terrain case, the deficit has already been practically negligible at $20D$. The decay rate is even slower for the quasi-3D hill.

The increase of the turbulence level results in a faster flow recovery at long distances as expected. However, the wind speed deficit at hub height is not always monotonously decreasing. This is a result of the wake geometry modification when the turbulence level changes, which is more pronounced in the quasi-3D geometry for the $TI_{in} = 20\%$ case.

In the flat terrain case, the wake centre is about $0.05D$ lower than hub height at $1D$ downstream and about $0.1D$ at $5D$ downstream. In the axisymmetric and the quasi-3D hill cases, the height difference between wake centre and hub is larger, about $0.15D$ and $0.2D$ at $1D$ and $5D$ downstream, respectively. For the $TI_{in} = 20\%$ case, the circular shape of the wake geometry has already been distorted at $5D$ downstream.

The effect of the wind direction on the decay rate of deficit is drastic. A change in the wind direction from 0 to 30° increases the decay rate in such a degree that it becomes comparable to that of flat terrain. For the 30° case, the wind speed deficit is practically negligible after $20D$. The height of the maximum deficit remains constant denoting similar wake geometry in the near wake. As the wind direction changes from 0 to 30° , a wider spreading of the wake is observed at long distances.

The predictions for the 3D axisymmetric hill with steep slope were also compared to those of two other models: Another Navier–Stokes model using $k-\varepsilon$ turbulence closure and the WASP model. The comparison in the velocity deficit and turbulence intensity between the two Navier–Stokes models can be considered good, whereas the WASP predicts reasonable velocity profile gradients and satisfactory deficit values for distances up to $11D$.

6. References

- [1] Chaviaropoulos, P. K. and Douvikas, D. I., (1998), "Mean-flow-field Simulations over Complex Terrain Using a 3D Reynolds Averaged Navier–Stokes Solver", Proceedings of ECCOMAS '98, Vol. I, Part II, pp. 842-848
- [2] Wilcox, D. C., (1993), Turbulence Modelling for CFD, DCW Industries Inc., La Canada, California, ISBN 0-9636051-0-0
- [3] Troen, I., Petersen, E. L., (1989), "European Wind Atlas," Risø National Laboratory, Roskilde, Denmark p 656
- [4] Mortensen, N. G., Heathfield, D. N., Myllerup, L., Landberg, L., Rathmann, O., (2005), "Wind Atlas Analysis and Application Program: WASP 8 Help Facility," Risø National Laboratory, Roskilde, Denmark
- [5] Troen, I., (1990), "A high resolution spectral model for flow in complex terrain", Ninth Symposium on Turbulence and Diffusion, Roskilde, April 30 – May 3, pp.417-420.
- [6] Jackson, P.S. and Hunt, J.C.R., (1975), "Turbulent flow over a low hill", *Q. J. Meteorol. Soc.* 101, pp.929-955.
- [7] Taylor, P.A., Walmsley, J.L., and Salmon, J.R., (1983), "A Simple Model of Neutrally Stratified Boundary-Layer Flow over Real Terrain Incorporating Wavenumber-Dependent Scaling", *Boundary-Layer Meteorol.* 26, pp.169-189.
- [8] Bowen, A. J., Mortensen, N. G., (1996), "Exploring the limits of WASP: the wind analysis and application programme", European Union Wind Energy Conference, H.S. Stephens and Associates, Bedford, UK, Goteborg.
- [9] Schepers, J. G., (2003), ENDOW: Validation and Improvement of ECN's Wake Model, Technical Report ECN-C-03-034, Energy Research Centre of the Netherlands

Appendix A

Derivation of the Relationship between the Inflow Turbulence Intensity at Hub Height and the Roughness Length

The turbulent kinetic energy, k , is defined as:

$$k = 0.5 (\sigma_x^2 + \sigma_y^2 + \sigma_z^2), \quad (\text{A-1})$$

where σ_x , σ_y and σ_z are the standard deviations of the wind speed fluctuations in directions x , y , z respectively. Taking into account the anisotropy of turbulence, $\sigma_y / \sigma_x = 0.8$ and $\sigma_z / \sigma_x = 0.5$, Eq. (A-1) becomes:

$$k = \sigma_x^2 f, \quad (\text{A-2})$$

with $f = 0.5(1 + (\sigma_y / \sigma_x)^2 + (\sigma_z / \sigma_x)^2) = 0.945$. Combination of Eq. (6) with Eq. (A-2) results in the relationship:

$$\sigma_x = 2.4135 u_*. \quad (\text{A-3})$$

The inflow turbulence intensity at hub height, TI_{in} , is defined as $TI_{in} = \sigma_x / U_{in}$, with U_{in} being the local inflow wind speed. Using this definition, Eq. (A-3) can be written as:

$$\frac{U_{in}}{u_*} = \frac{2.4135}{TI_{in}}. \quad (\text{A-4})$$

By substituting Eq. (A-4) into the logarithmic inflow wind speed profile given by Eq. (3), it follows that:

$$\frac{2.4135}{TI_{in}} = \frac{1}{K} \ln \left(\frac{z_{hub}}{z_0} \right) \quad \text{or} \quad z_0 = z_{hub} e^{-0.9895 / TI_{in}}, \quad (\text{A5})$$

which relates the inflow turbulence intensity TI_{in} at hub height z_{hub} with the roughness length z_0 .

Appendix B

Derivation of the Relationship between Turbulent Kinetic Energy and Turbulence Intensity

For the free stream flow, the turbulence intensity in x-direction is given by:

$$TI_x(z) = \sigma_x / U_x(z) , \quad (B-1)$$

where σ_x is the standard deviation of the wind speed fluctuations in x-direction and U_x is a function of height only, See Eq. (3).

In the wake region, the turbulence intensity is given by:

$$TI_{x,w}(y, z) = \sigma_{xw}(y, z) / U_x(z) , \quad (B-2)$$

namely the standard deviation of the wind speed fluctuations is again normalized with the free stream wind speed and not the local wake wind speed. Thus, added turbulence intensity is defined, which is a measure for the increase in standard deviation:

$$TI_{add,x}(y, z) = \sqrt{TI_{w,x}(y, z)^2 - TI_x(z)^2} = 1/U_x \sqrt{\sigma_{w,x}(y, z)^2 - \sigma_x(z)^2} \quad (B-3)$$

Considering the anisotropy of turbulence for the basic atmosphere, Eq. (A-2) is valid and can be rewritten as:

$$TI_x(z) = 1.026\sqrt{k(z)} / U_x(z) , \quad (B-4)$$

where $k(z)$ is the turbulent kinetic energy in the free stream. The turbulent kinetic energy in the wake region has been increased by the added turbulence:

$$k_w(y, z) = k(z) + k_{add}(y, z) \quad (B-5)$$

If the added turbulence was also anisotropic, the turbulence intensity in the wake should be given by Eq. (B-4) with $k_w(y, z)$ instead of $k(z)$. However, measurements in wakes have shown lower values for turbulence intensity in x-direction than those obtained considering Eq. (A-2). Therefore, a fully isotropic turbulence is assumed in the wake. Thus, turbulence intensity in x-direction is decreased improving the agreement with measurements. The isotropic assumption implies that $k = 1.5\sigma_x^2$, $\sigma_x = \sigma_y = \sigma_z = 0.82\sqrt{k}$ and is adopted only for the added turbulence:

$$TI_{add,x}(y, z) = 0.82\sqrt{k_{add}(y, z)} / U_x(z) \quad (B-6)$$

The combination of equations (B-3) through (B-6) results in:

$$TI_{w,x}(y, z) = 1/U_x(z) \sqrt{0.6724 k_w(y, z) + 0.3803 k(z)} , \quad (B-7)$$

which is the relationship providing the turbulence intensity in the wake using the predicted turbulent kinetic energy $k_w(y, z)$. In this report, Eq. (B-7) is also used for the cases without W/T, so that the relation between the predicted turbulent kinetic energy and the turbulence intensity is uniform.